RECONSTRUCTING NEURONAL NETWORK DYNAMICS
USING DATA ASSIMILATION

by

Franz Hamilton
A Dissertation
Submitted to the
Graduate Faculty
of
George Mason University
In Partial fulfillment of
The Requirements for the Degree
of
Doctor of Philosophy
Electrical and Computer Engineering

Committee:

_____ Dr. Nathalia Peixoto, Dissertation Director

_____ Dr. Timothy Sauer, Committee Member

_____ Dr. John Cressman, Committee Member

_____ Dr. Andre Manitius, Committee Member

_____ Dr. Monson Hayes, Department Chair

_____ Dr. Kenneth Ball, Dean, The Volgenau School of Engineering

Date: _____ Spring Semester 2015
George Mason University
Fairfax, VA

Reconstructing Dynamics in Neuronal Networks Using Data Assimilation

A dissertation submitted in partial fulfillment of the requirements for the degree of Doctor of Philosophy at George Mason University

By

Franz Hamilton
Bachelor of Science
George Mason University, 2010

Director: Dr. Nathalia Peixoto, Associate Professor
Department of Electrical and Computer Engineering

Spring Semester 2015
George Mason University
Fairfax, VA

Dedication

I dedicate this dissertation to my family and friends who supported me in this pursuit of higher education.

Acknowledgments

I would like to thank my committee for all of their helpful comments and suggestions on how to improve this research. I would also like to give a special thanks to my advisers Nathalia Peixoto and Timothy Sauer. Their advice and guidance was essential to the success and quality of my work. Their mentorship has been critical to my development as a researcher and person.

Table of Contents

List of Tables

List of Figures

Abstract

RECONSTRUCTING DYNAMICS IN NEURONAL NETWORKS USING DATA ASSIMILATION

Franz Hamilton, PhD

George Mason University, 2015

Dissertation Director: Dr. Nathalia Peixoto

Understanding the dynamics of the *in vivo* brain under normal and diseased states is one of the great challenges of modern scientific study. The overall complexity and dimension of the brain though can make this problem intractable. In an effort to study these dynamics in a more controlled, manageable setting, *in vitro* experimental and computational models have developed. Additionally, the advancement of mathematical analysis and techniques has led to a prominent role for data-assisted modeling whereby experimental data is fused with computational models allowing for data-driven predictions.

The first part of this dissertation will demonstrate the utility of the microelectrode array *in vitro* platform for probing the dynamics of cultured spontaneously active neuronal networks. Specifically, the influences of electrical stimulation on network firing dynamics will be examined. A low frequency, electric field applied to the network through the culture media is shown to have a significant effect on the network's spontaneous firing behavior. This stimulating field, shown in model to be uniform and sub-threshold, significantly reduced the bursting in tested networks. Furthermore, the capability of the cultured networks to display characteristics of learning is explored. Administration of a high frequency training signal is demonstrated to significantly increase the response of networks to a low frequency

probing stimulation. This increased sensitivity is found 30-50 ms after stimulus suggesting a potentiation of a post-synaptic mechanism.

The traditional analysis in the first part of this dissertation relies solely on measures related to the recorded neuronal extracellular potential. However, to understand the full dynamical evolution of a system it is often imperative to have estimates of the unmeasured variables. The second part of this dissertation will demonstrate the development and use of data assimilation techniques for the reconstruction of unmeasured neuronal network dynamics. A statistical assimilation algorithm relying on nonlinear Kalman filtering is implemented for the purposes of identifying and tracking neuronal network connectivity. Once validated in model, this technique is used to find network connections in *in vitro* network recordings. Additionally, a substantial extension of the assimilation methodology is proposed to deal with the specific case of unmodeled variables, when training data from the variable is available. This method uses a stack of several, nonidentical copies of a physical model to jointly reconstruct the variable in question. This technique is implemented to accurately recover unmodeled ionic concentration dynamics from synthetic seizure datasets. The method is then used to reconstruct the extracellular potassium concentration in a neuronal culture.

Chapter 1: Introudction

Understanding the dynamics of the brain under normal and diseased states has been a topic of great interest to researchers across a variety of disciplines. Neurons are the core component of the brain, processing and transferring information between each other through electrical and chemical network interactions. The networks in the brain consist of billions of neurons leading to a problem that is both high in dimension and complexity. This can make the elucidation of underlying mechanisms behind neuorological phenomenon, such as epilepsy and spreading depression, difficult.

As a means of reducing the overall complexity of the problem, *in vitro* cultures can be considered as an experimental model of the *in vivo* system. Microelectrode arrays in particular have become a popular *in vitro* platform through which to probe the dynamics of cultured neuronal networks [1]. Since the first recordings of single unit activity from snail neurons by Gross and collaborators [2, 3], the technology and use of microelectrode arrays to investigate different properties of neuronal networks has expanded significantly. Their capability to record spontaneous activity of multiple neurons in a network have made them ideal for application as a biosensor [4], for studies examining the effects of pharmacology and toxicology [5, 6] and for understanding the effects of electrical stimulation on network behavior [7–14]. Their utility however is limited to measurements of the neuronal extracellular potential, leaving all other dynamical variables as unobserved quantities.

Parallel to the growth of *in vitro* experimental models has been the development of nonlinear mathematical models descrbing the dynamics of neurons. The most famous of these is the Hodgkin-Huxley model [15]. The Hodgkin-Huxley equations describe the initiation and propagation of action potentials in a single neuron as a function of variables representing the neuronal membrane potential, gating variable dynamics and bio-plausible

parameter values. There have been several extensions of the Hodgkin-Huxley model, for example in describing the dynamics of neuronal seizures [16].

While biophysically accurate, the Hodgkin-Huxley model is computationally demanding particularly when considering a network-level implementation. In an effort to reduce computational complexity, numerous reduced-order models have developed making network analysis feasible. The Fitzhugh-Nagumo model [17,18] is one such model, serving as a direct simplification of the Hodgkin-Huxley equations. Additional simple models have developed including Wilson-Cowan [19], Hindmarsh-Rose [20] and Izhikevich model [21] to name a few.

The rapid expansion of technology in the physical sciences, allowing for the collection of large amounts of data, combined with the advancement of mathemical modelling has led to a surge in the use of data-assisted modeling. Data-assisted modeling represents a fusion of experimental study with traditional mathematical modeling. Data collected from a physical system is fit to a mathematical model through a data assimilation algorithm and unobserved variables are estimated. Its use has become standard in numerical weather prediction [22–25], oceanography [26] and various areas of spatiotemporal dynamics [27–30].

In the seminal work by Ullah and Schiff [31], the assimilation framework was used for the analysis of single-cell seizure recordings. Using a biophysically accurate seizure model, the authors were able to assimilate the measured potential from an *vitro* neuronal cell in seizure and reconstruct the neuron's sodium and potassium concentration dynamics as well as cell-specific parameter values. This was the first successful demonstration of the feasibility of data assimilation analysis of neuronal data [31].

The goal of this dissertation is twofold. The first part will demonstrate the use of the microelectrode array platform to investigate the effects of electrical stimulation on cortical neuronal networks. Our motivation here is to examine how we can use stimulation to alter the network firing dynamics of the cultured neurons. The analysis in this part will rely on traditional metrics based on the recorded extracellular potential.

In Chapter 3, we examine the influence of sub-threshold electric fields on neuronal

network activity. Endogenous fields found in the *in vivo* brain are low frequency and sub-threshold electric fields hypothesized to play a significant role in guiding cortical activity [12]. Using two silver/silver chloride electrodes we applied a low frequency stimulation to the culture bath, resulting in a homogenous sub-threshold stimulating field that was characteristically similar to *in vivo* endogenous fields. This stimulating field was found to significantly reduce the network's spontaneous bursting activity.

In Chapter 4 we assess the capability of cultured cortical networks to display characteristics indicative of learning. Expanding on the work done in [32], we explored the effects of a high frequency training signal on a network's response to a low frequency probing stimulation pulse. We found that administration of the training signal caused a significant increase in the network response to the stimulation, particularly in the timeframe of 30-50 ms after stimulation. These results suggest the potentiation of an early post-synaptic mechanism.

The second part of this dissertation focuses on the use of data assimilation for reconstructing network dynamics from the microelectrode array networks. As previously mentioned, while the array technology has been used in a wide variety of studies its measurements are limited to the neuronal extracellular potential. However, to fully understand the dynamical evolution of the system it's important that we have estimates of the unobserved system dynamics. Our focus here is the use of data assimilation techniques for reconstructing unobserved variables in neuronal networks. Since our analysis is focused on network data, a significant feature of this work will be the use of computationally simple models to assimilate the network measurements and estimate complex features.

In Chapter 6 we address the issue of network connectivity. We develop a statistical method for identifying and tracking network connectivity using a nonlinear data assimilation technique and the recorded neuronal potential. We demonstrate that our method can statistically identify the network connectivity and track any connection parameters that may vary over time due to network nonstationarity. Once this technique is validated on synthetic network data, it is implemented on recordings from spontaneously active *in vitro* networks.

In chapter 7 we develop a significant extension of the traditional data assimilation algorithm for the reconstruction of "unmodeled variables", or variables that do not appear in the equations of the model. Using a stacked set of parameterically different assimilation models, we demonstrate the ability of this technique to reconstruct complex ionic dynamics from a seizure dataset. We then implement this approach for the reconstruction and tracking of extracellular potassium concentration changes in an *in vitro* neuronal network.

Chapter 2: *In Vitro* Cultures on Microelectrode Arrays

2.1 Cell Culturing on Microelectrode Arrays

Cortical and spinal cord neurons were extracted from embryonic day 17 (E17) mice removed from a time-pregnant mouse. After enzymatic and mechanical dissociation, cells were plated on 64-channel microelectrode arrays (MEA) at a density of approximately 150,000-200,000 cells per array. Figure 2.1 shows a schematic of the *in vitro* culture preparation, the details of which can be found in [6]. Cultures were maintained in DMEM supplemented with horse serum, fetal bovine serum, B-27, and ascorbic acid for the first two days. At day 3, serum was removed and networks were maintained by a 50% media exchange twice a week. Dishes are handled in a biological hood when necessary to maintain sterility and are checked periodically under an inverted microscope for signs of contamination as well as homogeneous array coverage. Arrays that showed contamination are washed and sterilized. Cultures were incubated under controlled temperature, 37°C, and humidity, 10% CO_2. Figure 2.2 shows an example of a cultured MEA network.

2.2 Extracellular Recordings

MEAs allow for the simultaneous recording of neuronal extracellular potential at each of the array's electrodes. MEAs were hooked up to a Multichannel Systems (MCS) recording system (Reutlingen, Germany) and temperature was maintained at 35° C through a temperature control box (TC02 Temperature Controller Multichannel Systems, Reutlingen, Germany). Signals were acquired at a rate of 25 kHz and bandpass filtered from 300 Hz to 3 kHz. Figure 2.3 shows the filtered extracellular potential recorded at an MEA electrode. To account for any transient behavior caused by the movement of the culture

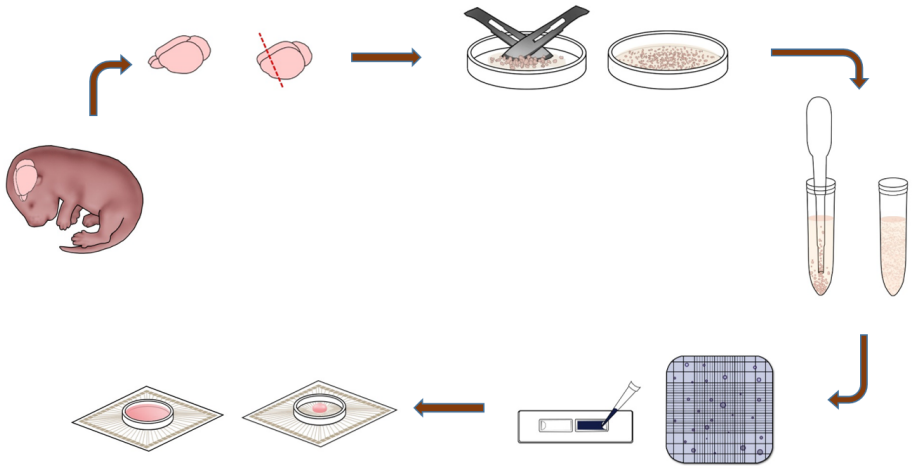

Figure 2.1: Generalized procedure for the preparation of *in vitro* arrays. Cortical and spinal cord neuronal cells are extracted from the embryos of time-pregnant mice. After the dissociation process, cells are plated onto MEAs at a density of approximately 150,000-200,000 cells per array depending on tissue type.

and subsequent hook up to the system, an initial stabilization period was alloted for all networks prior to recording or experimentation.

Data acquisition from the MEA comes in two forms: the raw time series of the extracellular potential and the calculated spike times from each electrode. A "spike" is declared when the extracellular potential crosses a pre-defined threshold. Thresholds for spike detection were set individually for each electrode by the recording software (MC Rack) to 5 standard deviations of the base electrode noise level. This value for standard deviation was determined to be optimal through numerous observations of MEA recordings in our laboratory. After thresholding, a spike train for each electrode is produced.

The dissociated cultures are spontaneously active, with a typical active electrode from a network displaying a spontaneous firing rate of approximately 10 Hz or around 600 spikes per minute. Depending on the tissue type of the culture, activity patterns can vary greatly. Figure 2.4 shows raster plot representation of the spontaneous activity from a representative spinal cord (Figure 2.4a) and cortical (Figure 2.4b) network.

Due to the physical architecture of the array, it is possible for a single electrode site to

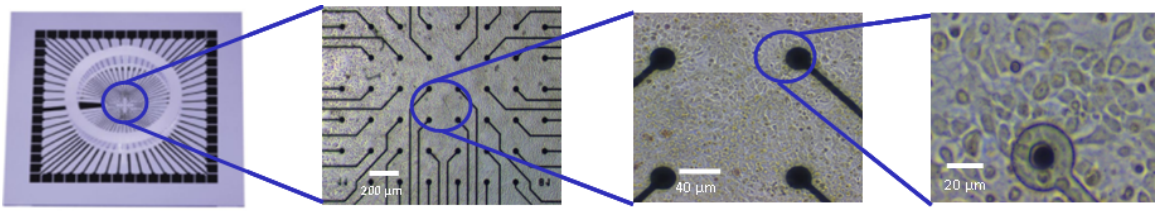

Figure 2.2: *In vitro* neuronal network cultured on a microelectrode array (MEA). The MEA is plated with E17 frontal cortex or spinal cord cells at a density of 150,000-200,000 cells per array. Cultures are incubated at 37°C with 10% CO_2 and maintained by a 50% media exchange twice a week between recording sessions or experimentation.

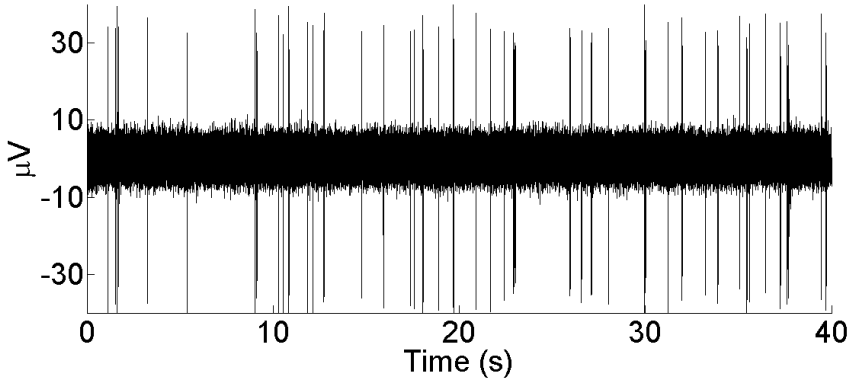

Figure 2.3: Extracellular time series recording from an active electrode from a cultured network.

record signals from multiple neurons. This implies that each electrode can be considered as a neuronal ensemble. However, post processing of the data allows for sorting of the signals into distinct neuronal units. Figure 2.5 shows an example of a multiple unit recording from a single electrode.

2.3 Optimal Timeframe for Network Recording and Experimentation

The identification of the optimal developmental age for dissociated cultures in terms of network activity and stability has been the topic of several studies, for example in Chiappalone

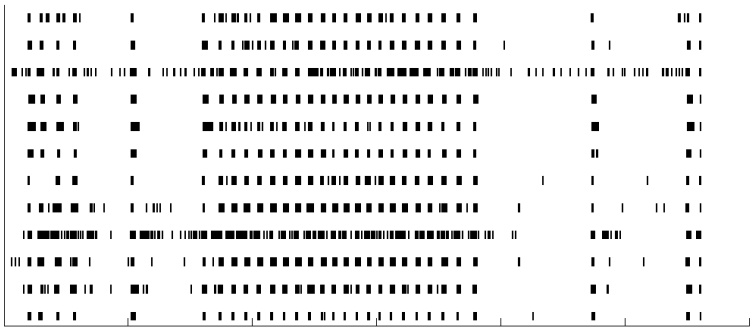

(a)

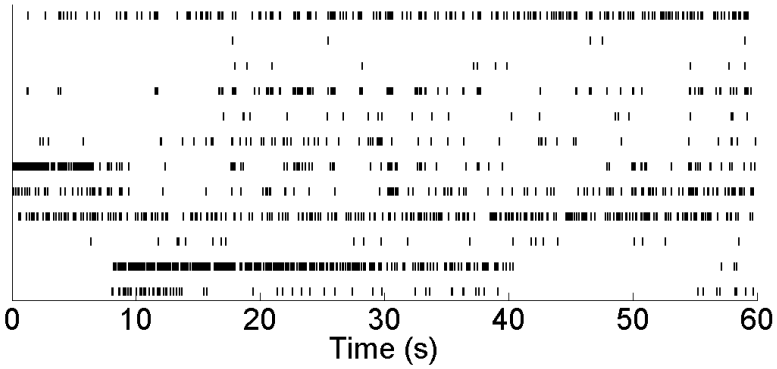

(b)

Figure 2.4: Typical spontaneous activity from an *in vitro* (a) cortical network and (b) spinal cord network. The patterns of activity between the two tissue types is vastly different. Spinal cord networks display a more stochastic firing pattern whereas cortical network activity appears to be driven by regular synchronized bursting events.

et. al [33]. They found that in their *in vitro* cortical cultures, the fourth and fifth weeks of culture development were ideal from the standpoint of stable, robust network activity. Given the procedural differences between individual labs, we tracked the development of several cultures plated by our lab to determine the optimal experimental period for our networks and see if our results matched those from the literature.

The network activity from 10 cultured MEA networks (5 cortical and 5 spinal cord) was tracked over their respective days *in vitro* (DIV) development. In general during the early stages of culture development (DIV 7-DIV 14), the networks are highly susceptible to changes in CO_2 resulting in a slow decline in spontaneous activity during prolonged periods

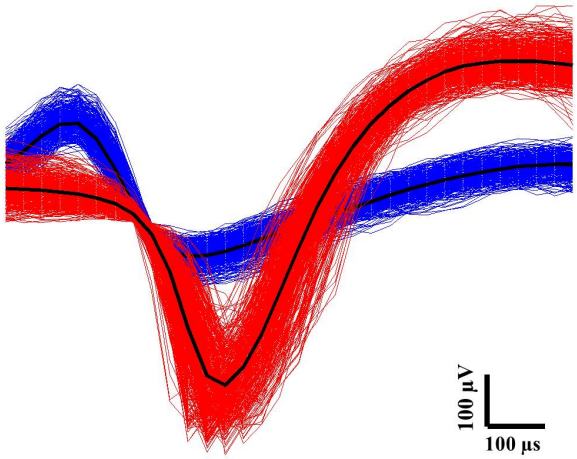

Figure 2.5: Sorted neuronal waveforms recorded from a single electrode site. Distinct difference in shape of waveforms suggests that each is representative of a different neuron.

outsides the incubator. As the cultures continue their development they become more robust to environmental changes making extended recording sessions possible. Addiitonally we observed a steady increase in the spontaneous network activity. Figure 2.6 shows the average network activity of a representative cortical network as a function of its *in vitro* developmental stage. Peak activity for this network (and in general all of our networks) occurs in the DIV 21-28 range. Taking our observations from our networks and the results from the literature into account, we targeted cultures aged DIV 28 or greater as the ideal time point at which to do our recording and experimentation.

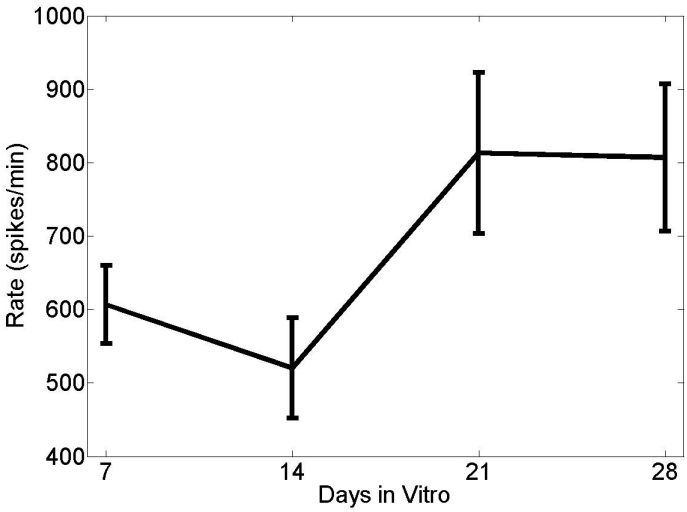

Figure 2.6: Multiple recordings from a representative MEA network plated with cortical neurons. At each DIV spontaneous activity was recorded from the network for 30 minutes. Error bars represent standard error amongst active network channels.

Chapter 3: Suppression of Neuronal Bursting through Electrical Fields

The following chapter has been published here [34].

Stimulation of neuronal networks has proven to be effective in changing neuronal behavior, such as bursting [7, 10, 11]. However, conducting neuronal stimulation through electric fields would provide an environment more similar to naturally occurring endogenous fields within the brain. These endogenous fields are low frequency and sub-threshold electric fields hypothesized to play a significant role in guiding cortical activity [12]. It has been demonstrated that the application of relatively low frequency (1-50 Hz) electric fields could modulate neuronal activity while the stimulation was active, entraining neuronal firing to the oscillations of the stimulating field. When the field was turned off, activity returned to its non-entrained state [12–14, 35].

In this chapter, we further explore the influence of electric fields on neuronal activity. *In vitro* networks of cortical neurons plated on MEAs were stimulated with electric fields through the arrays bath. This stimulation setup was chosen due to its robustness to various experimental designs. Results from a finite element modeling simulation determined that the stimulating field was sub-threshold and distributed homogenously throughout the network. The electric fields generated were characteristically similar to endogenous fields in the brain, oscillating at a low frequency and sub-threshold in strength. In particular, the effects on network bursting were examined. Network burst parameters were calculated and used to determine any influence of stimulation on the networks dynamics. Network activity was examined up to half an hour after stimulation in order to ascertain whether or not a persistent change occurred.

The percent change of burst parameters as compared to baseline values were calculated

for all MEA networks. Results showed a statistically significant difference between stimulated and control networks for the percent change in the number of bursts as well as interval between bursts. This supports the notion that we were able to change the dynamical behavior of the network, essentially steering the network from a high frequency bursting state to a low frequency bursting state.

3.1 Materials and Methods

In vitro cultures were prepared as described in Chapter 2. Our experimental protocol consisted of three periods: baseline recording, treatment period and post-treatment recording. A 30 minute baseline recording of spontaneous network activity was established. Networks (n = 5) then underwent ten minutes of field stimulation. A continuous low frequency sinusoidal wave, 1 Hz and 1 V peak-to-peak (Vpp), was applied to the networks with an Agilent 33220A function generator (Agilent, Santa Clara, CA) through two silver/silver chloride (Ag/AgCl) electrodes placed into the media of the MEA well. Immediately after the stimulation period, a 30 minute post-treatment recording of the networks spontaneous activity was obtained to determine if a persistent change in the network behavior occurred. Additional control networks (n = 4) went through the same protocol except that they did not receive any electrical stimulations.

Burst analysis was conducted for each active electrode in a network. A burst can be described as a sequence of action potentials whose interspike interval (ISI) is less than some determined threshold. Burst definition was done as detailed in [36]. After examining the distribution of the network logISI, a burst was characterized as at least five spikes with an ISI of at most 100 ms. Once initiated, a burst terminated when an ISI greater than 100 ms occurred.

To quantify a networks bursting behavior interburst interval (IBI), burst duration and total number of bursts were calculated for each channel. Outliers were removed if they were at least two standard deviations from the mean. Each channel was normalized to

its network average during baseline. These normalized values were then averaged within a network. Percent change from baseline was compared between stimulated networks and control networks using a Wilcoxon rank-sum statistical test. This analysis was done for each of the three burst measures.

To determine the strength of the stimulation that reached the neurons a 2-D finite element model (COMSOL, Burlington, MA) was developed. The MEA well was modeled as a rectangle (3 mm $\times$ 35 mm) which contained cell culture media with permittivity of 80 and conductivity of 1.38 S/m [37, 38]. Stimulating and reference electrodes were modeled as two bars, 1 cm apart, each having 200 μm width and 2 mm height. Only 400 μm of the electrodes were immersed in the cell culture media. The distance between electrode tips and the center bottom of the well was 2590 μm. The conductivity and permittivity of the electrodes were 6e7 S/m and 1, respectively. For sake of simplicity, the electric field was calculated at the center bottom of the well where the neurons were persumably located.

3.2 Results

In the bath stimulation setup, the electric field can be calculated by the equation below:

$$E = -\nabla V$$

where E is the generated electric field and ∇V is the gradient of the potential [39]. This differential equation was simulated as the governing physics in COMSOL given the described model setup in the Methods section. The resulting electric field generated throughout the MEA chamber when the stimulation was applied to the bath can be seen in Figure 2a. While the field strength varies throughout, within a 100 μm radius of the center of the array the electric field was homogeneous. This region of the MEA is where the neuronal cells were plated. Restricting our attention to this 200 μm diameter, the generated field was approximately 79.2 μV/μm (Fig. 2b), which implied that a typical 10 μm cell was exposed to 0.792 mV. Such an external field was considered sub-threshold from the perspective of a

Table 3.1:

Network	No. Networks	No. Bursts (%)	IBI (%)	Burst Duration (%)
Control	4	$-17 \pm 4\%$	$+15 \pm 0.07\%$	$-3 \pm 6\%$
Stimulated	5	$-70 \pm 10\%$	$+660 \pm 244\%$	$-43 \pm 15\%$

Summary of stimulation results. Reported values indicate average percentage change in dynamical measure (number of bursts, IBI, burst duration) as compared to baseline. (-) indicates a decreasing percentage and (+) indicates an increasing percentage. (*) indicates a statistically significant difference ($p < 0.05$) between the percent change as compared to baseline between stimulated networks and control networks. Statistical analysis showed significance for the difference in percentage change of number of bursts and IBI. This suggests that the applied field stimulation suppressed the spontaneous network bursting.

neuronal cell in the cortex, validating the stimulation setup.

The percent change in number of bursts, IBI and burst duration, as compared to baseline, were calculated for stimulated and control networks. Stimulated cortical networks exhibited a decrease in the number of spontaneous bursting events after stimulation as compared to baseline. In contrast, control networks did not show any noticeable difference. Raster plots showing this effect in a representative control and stimulated network can be seen in Fig. 3a and Fig. 3b respectively. The data showed that networks which received stimulation significantly decreased the number of bursts compared to control networks Ws = -2.45, $p < 0.05$. There was also a significant increase in IBI for stimulated networks compared to controls Ws = -2.45, $p < 0.05$. However, there was no significant difference between stimulated networks and controls for burst duration, Ws = -1.60. A detailed description of these results is summarized in Table 1.

3.3 Discussion

By applying a sub-threshold electric field to several cortical networks in vitro we were able to change the fundamental dynamics of the system. Specifically, the networks in a state of

high frequency bursting were shifted to a state of low frequency bursting. Such a change manifested itself in a decrease in number of bursts and an increase in the IBI. These changes were observed after stimulation had ended, showing a persistent effect of the stimulation on the network dynamics.

Using a stimulating electric field similar to biologically occurring endogenous fields would be a natural way to alter the firing dynamics of neuronal networks. Besides the benefit of having similar features to a biological phenomenon, the sub-threshold nature of the field would ensure that there are no adverse effects from the stimulation process. The COMSOL simulation confirmed that the area over the recording grid where neurons can be found was exposed to a sub-threshold electric field. This suggests that the observed decrease in spontaneous network bursting was the result of an actual change in the network dynamics caused by exposure to the electric field rather than the result of a stimulation-induced excitotoxicity.

3.4 Conclusion

We have demonstrated that sub-threshold electric field stimulation can be used to change the dynamical behavior of neuronal networks. Networks of cortical neurons cultured on MEAs in vitro were administered a 1 Hz 1 Vpp stimulation through the bath. The resulting electric field generated throughout the network was modeled by COMSOL, and this simulation verified that neurons in the network were exposed to a sub-threshold field. This stimulating field was shown to have a large impact on the dynamics of the neurons. Our results suggest a significant difference in percent change from baseline between stimulated networks and control networks for number of bursts and IBI. Specifically, the stimulating field showed the ability to suppress the spontaneous bursting of networks.

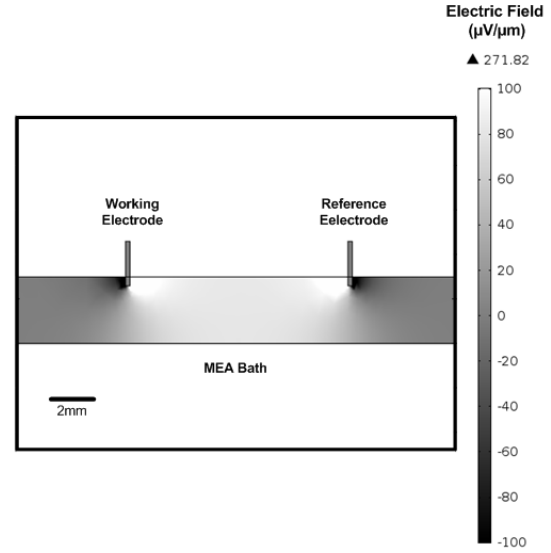

(a)

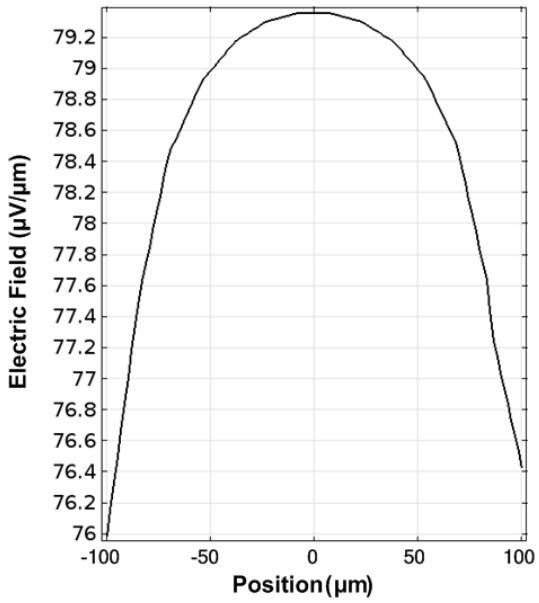

(b)

Figure 3.1: (a) Results of the COMSOL simulation of the electric field distribution throughout the MEA when the sinusoidal stimulation (1 Hz and 1 Vpp) was applied to the MEA bath through the Ag/AgCl electrodes. (b) Zoomed in results of the electric field over a 200 m length at the bottom center of the dish (denoted as 0) where the neuronal cells are plated.The resulting field generated in this region is approximately 79.3 μV/m. This implies that each 10 m cell is exposed to around 0.793 mV, validating the sub-threshold nature of the stimulating field.

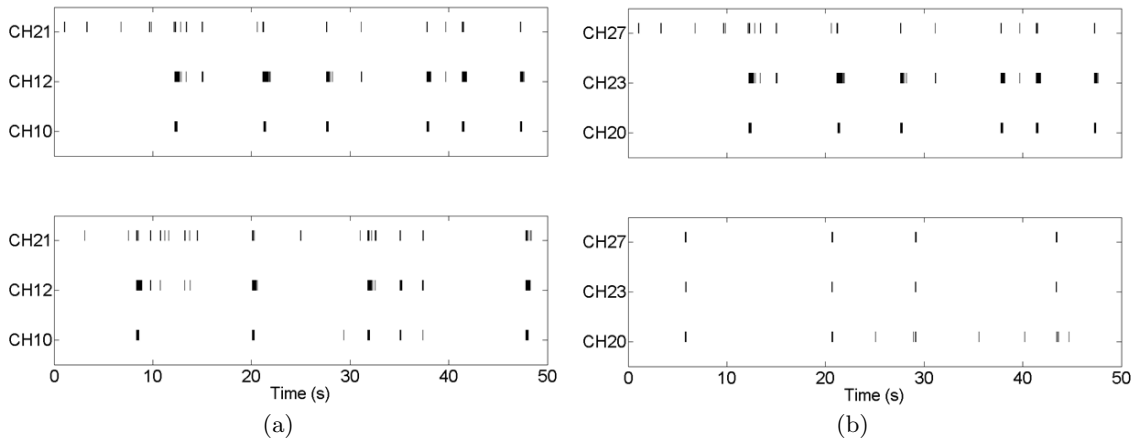

(a) (b)

Figure 3.2: (a) Raster plots displaying 50 seconds of spontaneous network activity from three active channels of a representative control network. Baseline activity (top) and post-treatment activity (bottom) after ten minutes of no stimulation. There were no visibly noticeable differences between these two periods. (b) Raster plots displaying 50 seconds of spontaneous network activity from three active channels of a representative stimulated network. Baseline activity (top) and post-treatment activity (bottom) after ten minutes of electric field stimulation. There was a noticeable suppression of network bursting after exposure to the sub-threshold field.

Chapter 4: Neuronal Training through Electrical Stimulation

The capability of *in vitro* cultures to display characteristics of learning would represent a significant development in the study development of memory. The use of electrical stimulation patterns to induce learning in neuronal cultures has been a topic of great interest in numerous studies, see for example [33, 40–45]. In Ruaro et al [32] it was suggested that cultured networks could be utilized as a tool for image processing based on their ability to discriminate between different configurations of stimulation electrodes representing spatial patterns. It was shown that network wide response to a spatial pattern in hippocampal cultures was significantly enhanced after a tetanization period suggesting successful induction of learning.

Our goal in this chapter is to expand on several of the findings in [32]. Here we investigated the effects of a high frequency training signal in networks of cortical neurons. Network response to a probing stimulation pulse was monitored before and after administration of the training signal. Results indicated an increase in network sensitivity to the probing stimulus after delivery of the training signal. This sensitivity manifested itself as an increase in network firing frequency and firing reliability immediately after the stimulus. This increase was found to be statistically significant in the time window of 30-50 ms after stimulation, suggesting potentiation of a post-synaptic mechanism.

4.1 Materials and Methods

4.1.1 Cell Culturing

Networks of cortical neurons were prepared on MEAs as described in Chapter 2.

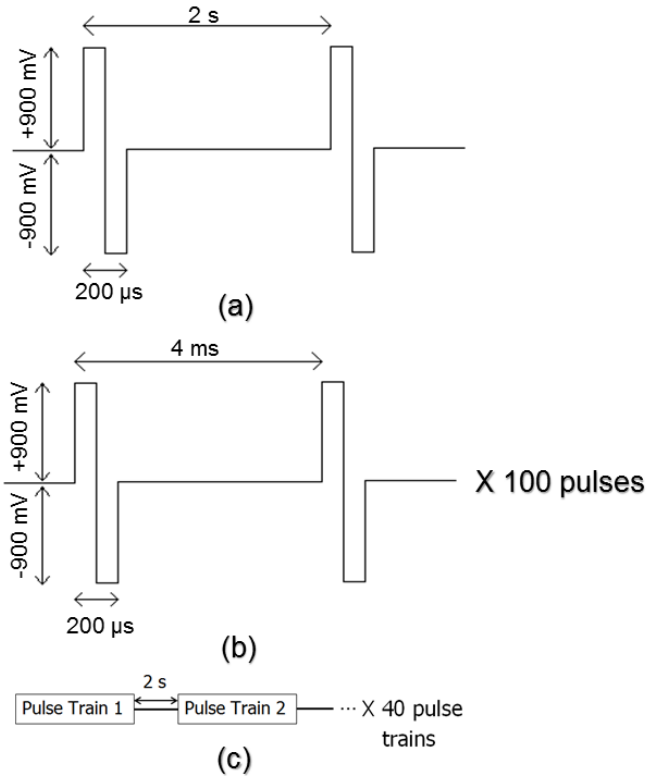

Figure 4.1: Parameters for probing stimulation and training signal. (a) Probing stimulation consisted of ± 900 mV bi-phasic pulses administered at a frequency of 0.5 Hz. Each phase lasted 100 μs for total pulse length of 200 μs. (b) Pulse trains consisted of 100, ± 900 mV bi-phasic pulses with frequency 250 Hz. (c) The training signal consisted of 40 total pulse trains administered at a frequency of 0.5 Hz.

4.1.2 Extracellular Recordings

Offline spike sorting was conducted prior to analysis to separate stimulation artifacts from neuronal signals at each electrode. Sorting was done using principle component analysis and a k-means algorithm. Identified biological signals were clustered together creating a neural assembly, or population response, at each electrode.

4.1.3 Stimulation

Electrical stimulation was applied to the culture through the electrodes using the commercially available stimulus generator STG 4002 (Multichannel Systems, Reutlingen, Germany).

Stimulating electrodes were not used for recording and therefore excluded from analysis. Thirteen electrode stimulation sites were selected in an "L" shape configuration, consisting of two perpendicular rows of electrodes meeting at a point. Parameters for both the probing stimulation and the training signal described below were defined as in [32].

Networks were administered five minutes of a probing stimulation (pre-training) through the selected stimulation sites. Probing stimulation consisted of a 0.5 Hz biphasic pulse, 200 μs pulse duration with 900 mV pulse amplitude. Figure 4.2a shows the parameters of the low frequency probing stimulation pulse.

After the pre-training stimulation phase, networks underwent a training procedure. The training signal was administered through the same electrodes as the probing stimulation. This high frequency signal (see Figure 4.2b-c) consisted of a 0.5 Hz pulse train with 40 total trains. Each train consisted of 100 biphasic pulses with 200 μs pulse duration, 900 mV pulse amplitude and 4 ms interpulse interval. Networks from $n = 12$ experiments received the training signal.

Once training was complete, five minutes of the probing stimulation (post-training) was re-administered to the networks.

A separate group of networks were treated as controls to control for possible changes in network response as a result of natural fluctuations or system nonstationarity. These networks underwent the same experimental protocol described above, with the exception that they received a sham training period and did not receive any training signal. Networks from $n = 10$ experiments received the sham training and were kept as controls.

4.1.4 Data Analysis

We examined the peristimulus time histogram (PSTH) for control and trained networks before and after the training period. Network activity was examined up to 50 ms after stimulus in 10 ms bins. The spike frequency in each bin was calculated individually for all active electrodes and averaged to give a network frequency per bin. In addition to spike frequency, spike reliability was calculated and averaged across all active electrodes to give

a network spike reliability per bin. Spike reliability can be interpreted as the probability of seeing a network response to the stimulation, where a maximum value of 1 indicates that there was a response to every stimulus pulse. All analysis was done using code developed in MATLAB^{TM} (MathWorks, Natick, MA).

To account for the variability amongst networks within a group, each network's post-training reliability and frequency were normalized with respect to their pre-training values. Any normalized value greater than 1 indicated an increase from pre to post-training and values less than 1 indicated a decrease. For example, we expected control networks to have normalized spike frequency and reliability values around 1 since they did not receive any training.

Statistical analysis between control and trained networks was carried out using a repeated measures one-way ANOVA with training (trained or control) as a between subject factor and time after stimulus (10-50 ms) as a within subject factor using SPSS (IBM, Armonk, NY). The Mauchly's test was carried out to determine if sphericity was violated. A Greenhouse-Geisser correction was used if sphericity was violated and significance was determined as $p < 0.05$. If a statistically significant interaction was found, a Tukey's post hoc analysis was run. All reported values are mean ± SEM.

4.2 Results

Figure 4.2 shows the activity response of eight active electrodes from a representative network that received training. The vertical red line indicates the time of a single stimulus pulse and the black lines denote neuronal activity in response to the stimulus. Figure 4.2a shows the network response pre-training and Figure 4.2b shows the response post-training. Pre-training the network exhibited an immediate response across channels to the stimulation within the first 20 ms after stimulus. However, the amount of activity after this initial response was inconsistent. Post-training, we observed a noticeable change in the network response. While the network still displayed the immediate response to the stimulus pulse within the first 10-20 ms, it also displayed a significant amount of activity 30-50 ms after

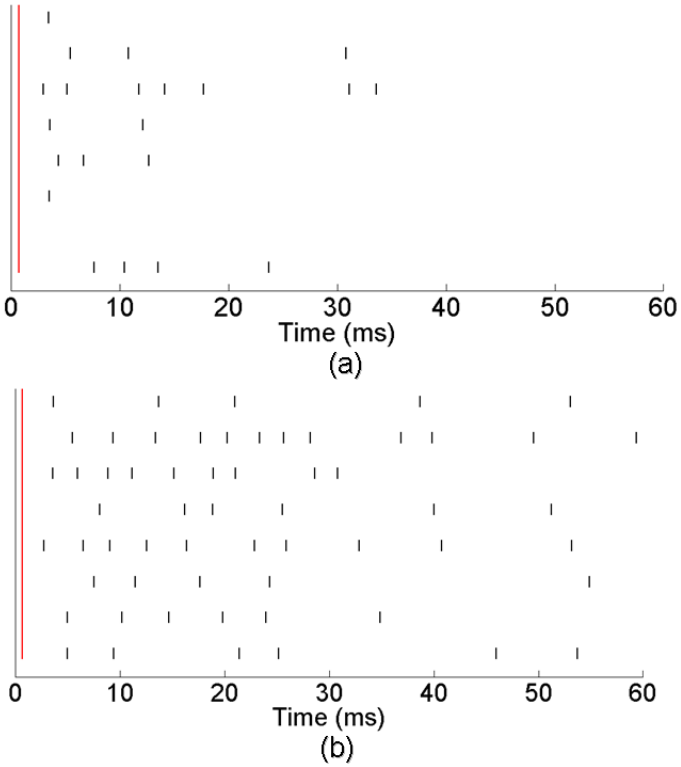

Figure 4.2: Activity response of eight active electrodes from a representative MEA network to a single stimulus pulse. Vertical red line indicates the time of the stimulus pulse and black lines denote neuronal spiking activity. Pre-training (a), we observe an immediate response across channels to the stimulus pulse. Post-training (b) we still witness this immediate response to the stimulation, however we also observe a more prolonged activity response.

stimulus.

Figure 4.3 shows the overall effect over the first 50 ms after stimulation between networks that received training compared to networks kept as controls for both normalized spike frequency and normalized reliability. (*) denotes statistical significance of $p < 0.05$. Analysis revealed that there was a statistically significant overall difference in spike frequency between trained networks and control networks ($F(1, 1.838) = 6.923, p < 0.05$). Specifically, the mean normalized spike rate for trained networks was 1.377 ± 0.090 and for control networks it was 1.024 ± 0.099. This meant that post-training, networks that received the training signal responded to the probing stimulus with 37% more activity than

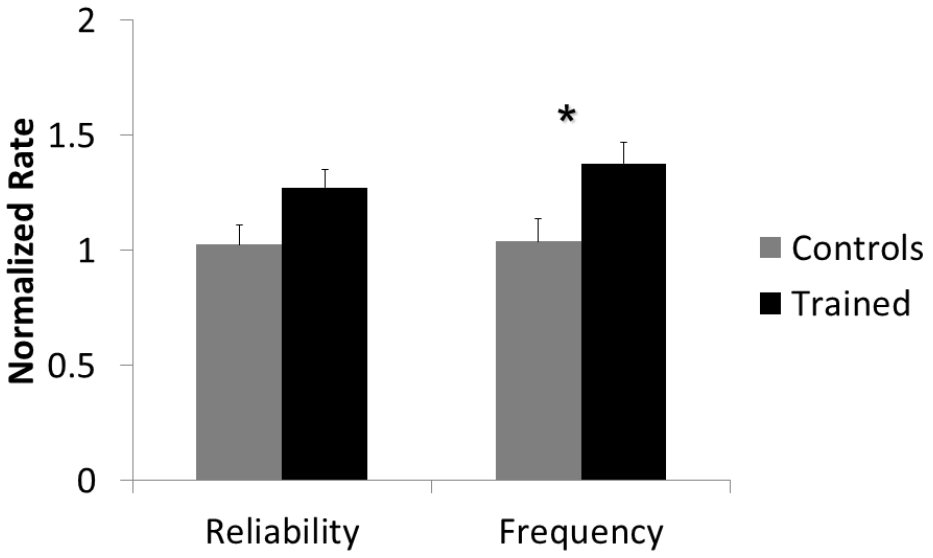

Figure 4.3: Mean normalized spike freqeuncy and spike reliability for networks that received training ($n = 12$) and networks that were kept as controls ($n = 10$). (*) denotes statistical significance $p < 0.05$. Statistical analysis indicated a statistically significant overall difference in spike frequency between trained groups when compared to control groups. There was no statistically significant overall difference in spike reliability.

they did pre-training. As expected, the response of control networks post-training did not differ greatly from their response pre-training. There was no statistically significant overall difference in spike reliability between the two groups.

Further analysis indicated a statistically significant interaction between spike frequency and time after stimulus($F(1, 1.838) = 4.290, p < 0.05$) and between spike reliability and time after stimulus ($F(1, 1.768) = 3.611, p < 0.05$). Figure 4.4 shows the normalized frequency and reliability of control and trained networks as a function of time after stimulus. A Tukey post-hoc analysis was run to determine the points of statistical significance. This post-hoc analysis indicated a statistically significant difference between spike frequency of control and trained networks at time bins 20-30 ms ($p < 0.01$), 30-40 ms ($p < 0.01$) and 40-50 ms ($p < 0.01$) after stimulus. Reliability between control and trained networks was also statistically different at time bins 20-30 ms ($p < 0.05$), 30-40 ms ($p < 0.01$) and 40-50 ms ($p < 0.01$).

There was approximately a 50% increase in spike frequency, as well as a 30-50% increase in spike reliability for trained networks in the range of 20-50 ms after stimulus. This large increase in network response in addition to the delayed effect suggests that the training fundamentally changed the network dynamics.

4.3 Discussion

The response of cultured networks to electrical stimulation can be broken down into multiple phases, allowing for a more thorough analysis of the changes in network response dynamics. The first phase is an early response of network activity within the first 20 ms after stimulus that is directly caused by the stimulation [7, 8, 46–49]. This direct response to the stimulation is driven electrically and not synaptically [46, 49] and is likely the result of electrical excitation of nearby axons [7, 8]. The second phase of the network response to stimulation is characterized by a burst of activity throughout the network, peaking between 20-200 ms after stimulation [46–49]. This activity propagation throughout the network after the immediate direct response relies on synaptic transmission [49].

Our results indicated that networks receiving the high frequency training signal developed a stronger response to the low frequency probing stimulation. This increased response was overall statistically significant as compared to control networks which received no training. Additionally, a statistically significant interaction effect was found between time after stimulus and whether or not a network received training. Follow-up post-hoc analysis indicated that networks receiving the training signal exhibited a statistically significant increase in spike frequency and spike reliability in the range of 20-50 ms after stimulation as compared to controls. This time window corresponds with the network response dynamics that are driven synaptically. This observed increase would therefore suggest that the effect of the training signal could be potentiation with a mechanism that is likely post-synaptic. The lack of a statistically significant difference between control and trained networks up to 20 ms after stimulus further reinforced the idea of synpatic potentiation, as the network response during this time is driven directly by the electrical stimulation and not by synaptic

mechanisms.

Our findings were somewhat consistent with those of [32] where the authors noted an overall increase in network response to a probing stimulation after the training period. However, the authors made no mention of any time-dependent effects like the ones observed in our study. The discrepancy in the results could be attributed to the functional difference in the cortical networks used here and the hippocampal networks used in [32].

4.4 Conclusion

We investigated the effects of a high frequency training signal on the response of cortical networks to a probing stimulation pulse. Results indicated that after receiving the training signal, networks responded with a statistically significant increase in spike frequency and spike reliability. The increase was found to be time-dependent, specifically in the time window of 30-50 ms after a stimulus pulse suggesting potentiation with a mechanism that is possibly post-synaptic.

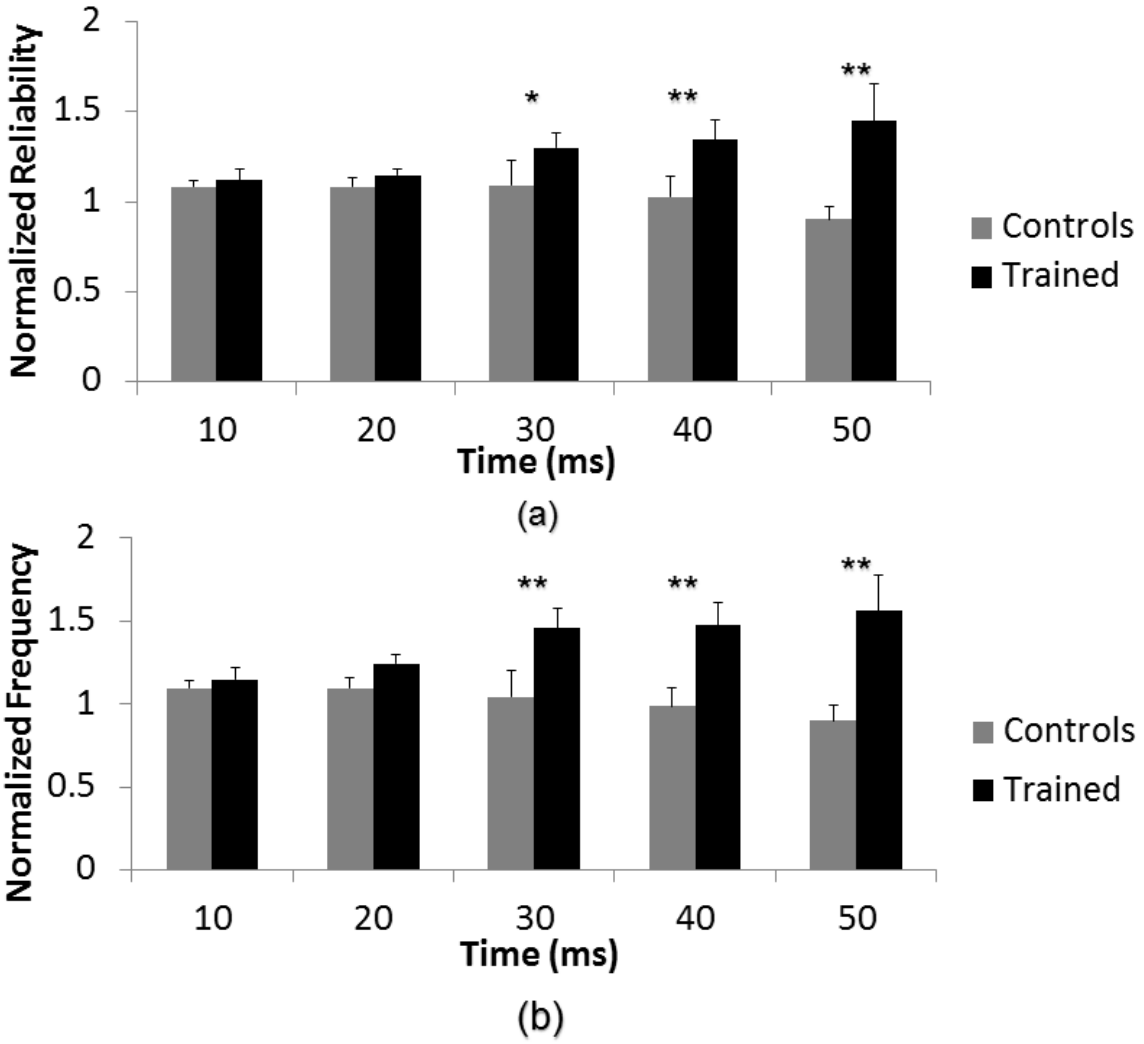

Figure 4.4: A statistically significant interaction between time after stimulus and training was found for both (a) spike reliability and (b) spike frequency ($p < 0.05$). A Tukey post-hoc analysis was run to determine the points of statistical significance. (**) denotes $p < 0.01$ significance and (*) denotes $p < 0.05$ significance. Post-hoc analysis showed that there was a statistically significant difference in normalized spike frequency and normalized spike reliability at time bins 20-30 ms, 30-40 ms and 40-50 ms after stimulus between trained and control networks.

Chapter 5: Data Assimilation for State and Parameter Estimation

5.1 The Mathematical Inverse Problem

In the study of physical systems we are often restricted by a limitation in our observations. What this means is that we are only able to measure a subset of variables from the system, leaving all others as unmeasured quantities. While the collected data are valuable, they give us an incomplete picture when trying to understand the full dynamical evolution of the system. The question is what additional information can we learn about the system given the collected data? This resulting mathematical inverse problem plays a crucial role in understanding the system dynamics.

We assume observation of a physical system in the time interval $[t_1, t_k]$ during which time we collect noisy measurements $y = [y_1, y_2, \ldots, y_k]$ from a measurable dynamic of the system. Our goal is to estimate and track the unmeasurable quantities of the physical system using a mathematical model.

Assume we have a parametrized n dimensional system of ordinary differential equations (ODEs) modelling the physical system

$$\begin{aligned} \dot{x}_1 &= f_1(x_1, x_2, \ldots, x_n, p_1, \ldots, p_m) \\ \dot{x}_2 &= f_2(x_1, x_2, \ldots, x_n, p_1, \ldots, p_m) \\ &\vdots \\ \dot{x}_n &= f_n(x_1, x_2, \ldots, x_n, p_1, \ldots, p_m) \end{aligned} \tag{5.1}$$

For notation purpose, we can rewrite (5.1) in vector form

$$\dot{x} = f(x, p, t) + w \tag{5.2}$$

f represents the dynamics of the model, x is an n-dimensional vector of state variables, p is a m-dimensional vector of parameters and w is a Gaussian noise term known as the dynamical noise. Dynamical noise can be thought of as the error between the equations of the model and the dynamics of the actual physical system. Some of the model parameters may be calculated through first principles or known from the literature, but frequently they are unknown quantities to be estimated.

We define a measurement or observation function h that maps x and p to a predicted measurement $\hat{y}$

$$\hat{y} = h(x, p, t) + v \tag{5.3}$$

where v is a Gaussian noise term known as the observational noise. The observational noise can be thought of as the error in the measurements introduced by sensor inaccuracy. We can also think of (5.1) and (5.3) as discrete-time processes which will help later in formulating the estimation algorithms

$$\begin{aligned} x_{k+1} &= f(x_k, p, t_k) + w_k \\ \hat{y}_k &= h(x_k, p, t_k) + v_k \end{aligned} \tag{5.4}$$

The idea behind the mathematical inverse problem is to find estimates for the state variables $\hat{x}$ and parameters $\hat{p}$ such that the predicted model observation $\hat{y}$ matches the measurements y as close as possible. In other words, we would like to minimize the residual $r = y - \hat{y} = [r_1, r_2, \ldots, r_k]$. There are two approaches to minimizing r leading to two general class of estimators: non-sequential and sequential estimation methods. In non-sequential estimation r is minimized at once. A popular non-sequential estimator is the

family of shooting methods, details of which can be found in [50–52]. On the other hand with sequential estimation each r_i is minimized individually. While there are advantages and disadvantages for both estimation approaches, the focus of this dissertation will be on use of sequential estimation in data-assisted modeling.

5.2 The Kalman Filter

Data assimilation is the process whereby easily measured, and often noisy, data are incorporated into a mathematical model of the system using a sequential estimation algorithm, such as the Kalman filter. The Kalman filter [53] employs a predictor-corrector methodology for state estimation. At time $k-1$ the filter makes a prediction, or *a priori* estimate, of the system's state and covariance at time k. After we take a measurement of the system at time k, the filter corrects the prediction making an *a posteriori* estimate of the state and covariance at time k. The basic idea of the Kalman filter is shown schematically in Figure 5.1.

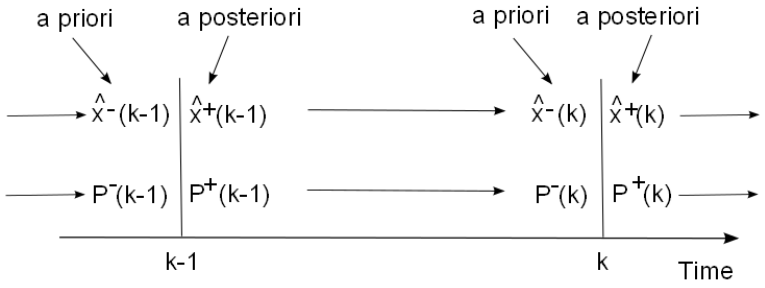

Figure 5.1: Schematic of the Kalman filter.

The underlying assumption of the Kalman filter is that the model represeting the physical system is linear. Specifically in (5.4) f and h are assumed to be linear transformations.

With that in mind, we assume the following linear discrete-time system

$$\begin{aligned} x_k &= F_{k-1}x_{k-1} + w_{k-1} \\ y_k &= H_k x_k + v_k \\ w_k &\sim (0, Q_k) \\ v_k &\sim (0, R_k) \end{aligned}$$

The Kalman filter equations are defined as follows

$$\begin{aligned} P_k^- &= F_{k-1}P_{k-1}^+ F_{k-1}^T + Q_{k-1} \\ K_k &= P_k^+ H_k^T R_k^{-1} \\ \hat{x}_k^- &= F_{k-1}\hat{x}_{k-1}^+ \\ \hat{x}_k^+ &= \hat{x}_k^- + K_k(y_k - H_k\hat{x}_k^-) \\ P_k^+ &= (I - K_k H_k)P_k^- \end{aligned}$$

where $\hat{x}_k^-$ and P_k^- are the estimates of the state and covariance prior to processing the measurement at time k and $\hat{x}_k^+$ and P_k^+ are the state and covariance estimates after processing the measurement at time k. Alternative forms of the Kalman filter equations can be derived for purposes of stability as well as ease of implementation. See Appendix A.1 for a useful derivation of an alternative form that will be helpful later when discussing nonlinear filtering techniques.

5.3 Nonlinear Filtering: The Ensemble Kalman Filter

Unfortunately the majority of physical systems, as well as the models representing them, are nonlinear meaning that outright application of the Kalman filter equations would lead to large errors in the estimates. In dealing with these systems, the goal is to find a way

to approximate the nonlinear system first before application of the linear Kalman filter equations. Advancements in nonlinear analysis and techniques have led to two prominent nonlinear Kalman filters in the literature: the extended Kalman filter and the ensemble Kalman filter. In the extended Kalman filter (EKF), the approximation of the nonlinear system is done through linearization. Rather than linearization, the ensemble Kalman filter (EnKF) [22] approximates the nonlinear system using a finite weighted ensemble whose mean and covariance preserve those of the system. The ensemble approach offers computational advantages (linearization at each filter step is computationally demanding) as well as higher order accuracy in its approximations, making it our method of choice. For a detailed discussion of the accuracy of both the linearization and ensemble approach, see Appendix A.2.

There are different approaches to selecting the ensemble, but the unscented transformation gives us a natural way to do so in the form of the defined sigma points. For an n dimensional nonlinear system, $2n$ sigma points sigma points are chosen though more can be defined so as to include higher order information about the sytem. Here, we restrict ourselves to $2n+1$ weighted sigma points where the additional sigma point is the current mean of the system. The ensemble is weighted such that

$$\sum_{i=0}^{2n} W^{(i)} = 1$$

We assume the discrete time system shown in (5.4)

$$\begin{aligned} x_{k+1} &= f(x_k, t_k, p) + w_k \\ y_k &= h(x_k, t_k, p) + v_k \\ w_k &\sim (0, Q) \\ v_k &\sim (0, R) \end{aligned}$$

where w and v are Gaussian noise terms with variances Q and R respectively and p is an m-dimensional vector of system parameters.

We initialize the filter with state vector $\hat{x}_0^+$ and covariance matrix $\hat{P}_0^+$. Without loss of generality we set

$$\begin{aligned} \hat{x}_0^+ &= 0_{n\times 1} \\ \hat{P}_0^+ &= I_{n\times n} \end{aligned}$$

where $0_{n\times 1}$ is an n vector of zeros and $I_{n\times n}$ is the $n \times n$ identity matrix. Using the theory behind the unscented transformation [54–56], we define $2n+1$ *ensemble* members such that

$$\begin{aligned} \hat{x}_{k-1}^0 &= \hat{x}_{k-1}^+ \\ \hat{x}_{k-1}^i &= \hat{x}_{k-1}^+ + \tilde{x}^i \qquad i = 1, \ldots, 2n \\ \tilde{x}^i &= \left(\sqrt{nP_x^+(k-1)}\right)_i^T \quad i = 1, \ldots, n \\ \tilde{x}^{n+i} &= -\left(\sqrt{nP_x^+(k-1)}\right)_i^T \; i = 1, \ldots, n \end{aligned}$$

where the square root shown above is the matrix square root that can be calculated calculated for example with the singular value decomposition (SVD) or Cholesky factorization.

We apply the dynamics f to the ensemble to move them forward in time from $k-1$ to k

$$\hat{x}_k^{(i)} = f\left(\hat{x}_{k-1}^i, t_{k-1}, p\right)$$

and from this calculate the *a priori*, or background, state at time k

$$\hat{x}_k^- = \sum_{i=0}^{2n} W^{(i)} \hat{x}_k^i$$

and the associated *a priori*, or background, covariance

$$P_k^- = \sum_{i=0}^{2n} W^i \left(\hat{x}_k^i - \hat{x}_k^-\right) \left(\hat{x}_k^i - \hat{x}_k^-\right)^T + Q$$

To each ensemble member at time k we apply the observation function

$$\hat{y}_k^i = h\left(\hat{x}_k^i, t_k, p\right)$$

and find the measurement predicted by our nonlinear model

$$\hat{y}_k = \sum_{i=0}^{2n} W^i \hat{y}_k^i$$

This allows us to construct the measurement covariance

$$P_k^y = \sum_{i=0}^{2n} W^i \left(\hat{y}_k^i - \hat{y}_k\right) \left(\hat{y}_k^i - \hat{y}_k\right)^T + R$$

and the cross-covariance

$$P_k^{xy} = \sum_{i=0}^{2n} W^i \left(\hat{x}_k^i - \hat{x}_k^-\right) \left(\hat{y}_k^i - \hat{y}_k\right)^T$$

We can now update our state and covariance estimates using the observation y_k and the

Kalman update given by

$$\begin{aligned} K_k &= P_k^{xy}(P_k^y)^{-1} \\ P_k^+ &= P_k^- - P_k^{xy}(P_k^y)^{-1}P_k^{yx} \\ x_k^+ &= x_k^- + K_k\left(y_k - y_k^-\right). \end{aligned}$$

5.4 Ensemble Kalman Filtering for State and Parameter Estimation

Thus far, the state estimation problem has been addressed specifically. However, in a typical data assimilation problem unknown model parameters need to be estimated in addition to the unknown state variables. This dual estimation problem [50, 57–59] can be addressed in a straightforward manner by extending the EnKF methodology.

To estimate the parameters along with the states of our model, we consider the state augmentation approach as discussed in [31, 50, 60–62]. With this method, we treat the m dimensional parameter vector p as extra states of the model that have trivial dynamics

$$\dot{p} = \begin{bmatrix} \dot{p}_1 \\ \dot{p}_2 \\ \vdots \\ \dot{p}_m \end{bmatrix} = \begin{bmatrix} 0 \\ 0 \\ \vdots \\ 0 \end{bmatrix}$$

This allows us to form an augmented state vector consisting of the original n model states

and m parameters

$$\hat{x} = \begin{bmatrix} x_1 \\ x_2 \\ \vdots \\ x_n \\ p_1 \\ p_2 \\ \vdots \\ p_m \end{bmatrix}$$

allowing for simultaneous state and parameter estimation

We demonstrate this dual estimation scheme in two example systems. Consider the Lorenz-63 system [63] perturbed by dynamical noise

$$\begin{aligned} \dot{x}_\eta &= \sigma(x_\eta - y_\eta) + \eta\dot{W}_x \\ \dot{y}_\eta &= x_\eta(\rho - z_\eta) - y_\eta + \eta\dot{W}_y \\ \dot{z}_\eta &= x_\eta y_\eta - \beta z_\eta + \eta\dot{W}_z \end{aligned} \tag{5.5}$$

where $\sigma = 10$, $\rho = 28$ and $\beta = \frac{8}{3}$. $\dot{W}$ represents uncorrelated white noise of unit variance and η represents the level of dynamical noise. For this example, we set $\eta = 1$. This system is simulated using a fourth-order Runge-Kutta with integration step-size $h = 0.05$ and our observation is limited to the x_η variable at sample rate $dt = 0.05$.

The goal of this state and parameter estimation problem is given observations of x_η, estimate the y_η and z_η state variables as well as the σ, ρ and β parameter values. We

provide the EnKF with the following assimilation model

$$\begin{aligned} \dot{x} &= \sigma(x-y) \\ \dot{y} &= x(\rho-z)-y \\ \dot{z} &= xy-\beta z \end{aligned} \tag{5.6}$$

and assume an observation function $h(x,y,z)=x$. Note the discrepancy in the observed physical system (5.5) and the model chosen for the filter (5.6). Since we are interested in the dual estimation problem, we can rewrite the filter model as

$$\begin{aligned} \dot{x} &= \sigma(x-y) \\ \dot{y} &= x(\rho-z)-y \\ \dot{z} &= xy-\beta z \\ \dot{\sigma} &= 0 \\ \dot{\rho} &= 0 \\ \dot{\beta} &= 0 \end{aligned}$$

In this augmented form, the EnKF is able to simultaneously estimate the state variables and parameters of (5.6).

The initialization of state and parameter values in the EnKF requires some discussion. In general initialization needs to be within a neighborhood of the correct values, meaning if you start too far away from the truth than the result can be convergence to incorrect estimates or filter divergence. The size of this neighborhood though is influenced by several factors including, amount of noise as well as the overall system dynamics (some systems are more sensitive to initialization than others, notably chaotic systems). Therefore the results of the estimation, including convergence time and the final estimated values, are dependent on several factors.

Figure 5.2 shows the results of the state and parameter estimation of the system described in (5.5) with filter initialization

$$\begin{bmatrix} x_0 \\ y_0 \\ z_0 \\ \sigma_0 \\ \rho_0 \\ \beta_0 \end{bmatrix} = \begin{bmatrix} 0 \\ 0 \\ 0 \\ 3 \\ 8 \\ 1 \end{bmatrix}$$

The estimated state variables in Figure 5.2a (color traces) do a good job of tracking the true system trajectories (black curves). However, there is notable error in the estimate of the z trajectory. This error can be explained by Figure 5.2b which shows the estimated parameter values (color traces) and the true parameter values (dotted black lines). There is a level of error in the parameter estimates, particularly for the ρ and β parameter values. Of note, the estimated parameter values converged, they just converged to slightly inaccurate values. This likely was a contributing factor to the error in the state variable estimates.

We now consider a second demonstrative example, the Hindmarsh-Rose system [20] influenced by dynamical noise

$$\begin{aligned} \dot{x}_\eta &= y_\eta - a x_\eta^3 + b x_\eta^2 - z_\eta + I + \eta \dot{W}_x \\ \dot{y}_\eta &= 1 - d x_\eta^2 - y_\eta + \eta \dot{W}_y \\ \dot{z}_\eta &= 0.005 \left[4 \left(x_\eta - \left(-\frac{8}{5} \right) \right) - z_\eta \right] + \eta \dot{W}_z \end{aligned} \tag{5.7}$$

where $a = 1$, $b = 3$, $d = 5$ and $I = 3.25$ (see [20] for different parameter values that generate various system behaviors). $\dot{W}$ represents uncorrelated white noise of unit variance and η represents the level of dynamical noise. For this example, we set $\eta = 0.1$. This system is

simulated using a fourth-order Runge-Kutta with integration step-size $h = 0.05$ and our observation is limited to the x_η variable at sample rate $dt = 0.05$.

Much like in the previous Lorenz-63 example, given observations of x_η our goal is to estimate state variables y_η and z_η and parameters a, b, and d (note: we assume that we have knowledge of the correct value for parameter I). We provide the EnKF with the following assimilation model

$$\begin{aligned} \dot{x} &= y - ax^3 + bx^2 - z + 3.25 \\ \dot{y} &= 1 - dx^2 - y \\ \dot{z} &= 0.005\left[4\left(x - \left(-\frac{8}{5}\right)\right) - z\right] \end{aligned} \tag{5.8}$$

with observation function $h(x, y, z) = x$. We re-formulate (5.8) for the dual estimation problem

$$\begin{aligned} \dot{x} &= y - ax^3 + bx^2 - z + 3.25 \\ \dot{y} &= 1 - dx^2 - y \\ \dot{z} &= 0.005\left[4\left(x - \left(-\frac{8}{5}\right)\right) - z\right] \\ \dot{a} &= 0 \\ \dot{b} &= 0 \\ \dot{d} &= 0 \end{aligned}$$

Figure 5.3 shows the results of the state and parameter estimation of the system described

in (5.7) with filter initialization

$$\begin{bmatrix} x_0 \\ y_0 \\ z_0 \\ a_0 \\ b_0 \\ d_0 \end{bmatrix} = \begin{bmatrix} 0 \\ 0 \\ 0 \\ 0 \\ 0 \\ 0 \end{bmatrix}$$

Figure 5.3a shows the results of the state variable estimation (color traces) compared to the true trajectories of the variables (black traces). Figure 5.3b shows the results of the parameter estimation (color traces) compared to the true parameter values (dotted black lines). We are able to estimate the general dynamics of the state variables as well as obtain fairly accurate parameter estimates, however there is some error in the estimation much like in the Lorenz-63 example.

Both examples show the capability of the EnKF to perform the simultaneous dual estimation of states and parameters. However, in both examples there were errors in the estimates. This shows that the state and parameter estimation problem, even in the case of a fairly well-known system, is far from trivial.

Of note, the results presented here are a reflection of the noise level η and the filter initialization used. As these change, one can expect slight variations in the results. For example, as η increases the estimation problem becomes much more difficult since the assumed assimilation model has a larger degree of model error. Also, if the filter initialization is done too far from the true system values then one could expect incorrect convergence or filter divergence.

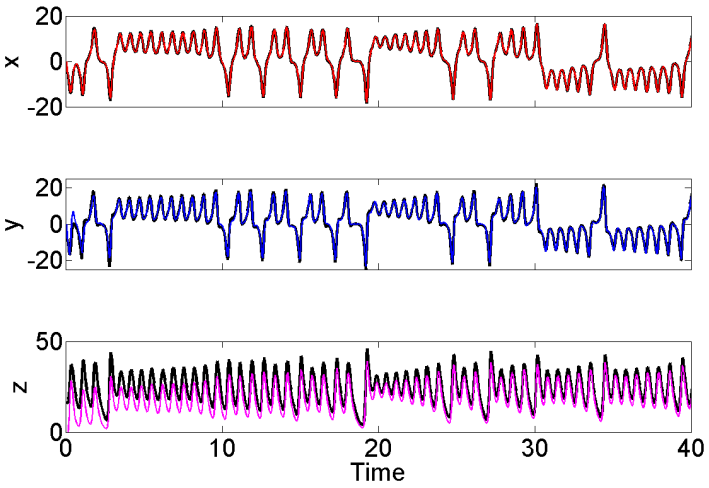

(a)

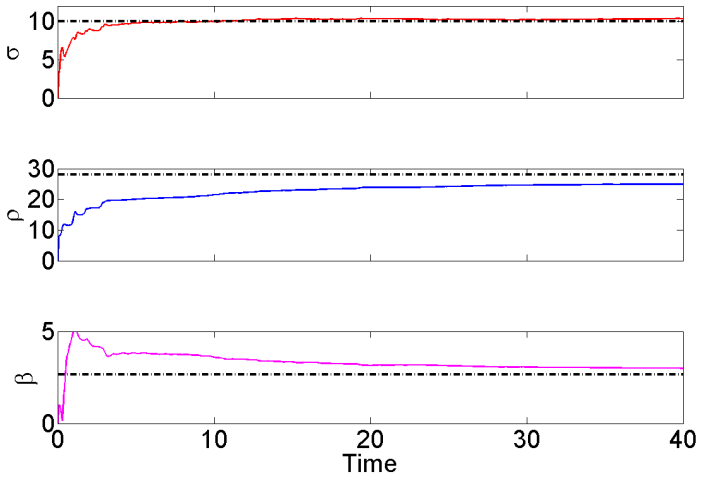

(b)

Figure 5.2: Results of EnKF estimation of (a) state variables and (b) parameters in the Lorenz system described by (5.5). (a) Black lines represent true trajectory of the system variables and colored lines denote filter estimate. (b) Dotted black lines denote true parameter values and colored lines denote filter estimate.

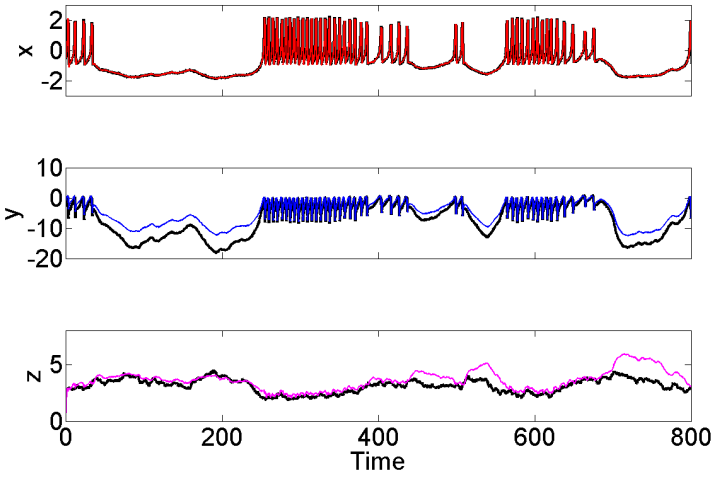

(a)

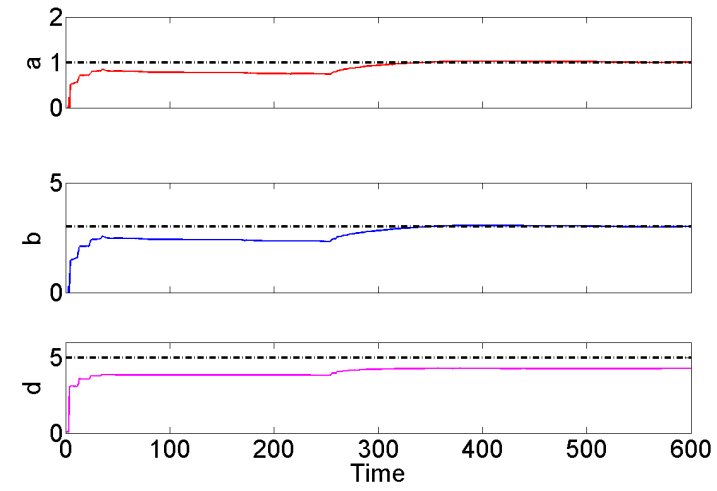

(b)

Figure 5.3: Results of EnKF estimation of (a) state variables and (b) parameters in the Hindmarsh-Rose system described by (5.7). (a) Black lines represent true trajectory of the system variables and colored lines denote filter estimate. (b) Dotted black lines denote true parameter values and colored lines denote filter estimate.

Chapter 6: Real-time Tracking of Neuronal Network Structure using Data Assimilation

The following chapter has been published here [62].

A dynamic of particular interest in neuronal networks is the connectivity structure. Connectivity changes as a function of network development and in response to applied electrical or pharmacological stimuli. Tracking these changes is essential for understanding the underlying dynamical evolution of the network, and serves as a valuable tool for experimental interventions.

A method for tracking connectivity should ideally meet several criteria. First, it should be statistical in nature. A strictly statistically-based method will require only a predetermined confidence level, removing the need to provide an arbitrary decision threshold or decide how to make conclusions from a ROC curve. Second, the method should be robust to error. We are typically interested in error caused by system noise, and error caused by a mismatch in dynamics between acquired data and the model used to represent the data. Third, the method should have sequential, or real-time, implementation capability. Real-time analysis of a network's structure is particularly important in experimental scenarios where feedback is critical for determining or controlling the direction of the experiment. This article describes a new method for tracking connectivity in neuronal networks that meets these three criteria.

Methods for detecting network links from complex time series have been the focus of several recent studies. The analysis of interactions between nonlinear processes was pursued in [64, 65], and ideas from compressed sensing were introduced in [66]. The concept of Granger causality [67] has been exploited by calculating partial directed coherence in [68].

Parallel to these developments are a wide range of connectivity methods for spike train measurements. Higher moment methods such as coherence, joint densities and cumulant

spectra were pursued in [69–71]. An information theory approach was proposed in [72]. Maximum likelihood methods for spike train neuronal interaction were investigated in [73–76]. These methods do not meet the first criteria of being statistically based.

The Cox method, introduced for neural networks in [77] and refined in [78], was the first statistical test for connectivity in networks analyzed by spike trains. The method was expanded in [79] to include a test for changes in connectivity. While the Cox method satisfies the first two criteria of being statistical and robust to error, it fails to meet the third. Data requirements were found in [79] to be at least 10^3 spikes per node, and prior to the conclusion of processing, the method provides no estimate of the network connectivity structure. Furthermore, if new data is acquired then the entire data set must be re-processed before it can be included in the estimate, making use of the Cox method more suitable for offline analysis.

In the following chapter we use of a parameter-augmented version of the EnKF to estimate connection strengths of a network of cultured neurons sampled by an MEA. The Kalman filter [53] is a natural choice for this problem, because in addition to estimating the connection parameters it will estimate their uncertainties, which will allow a statistical test for connectivity on acquired time series to be developed. We will show that the method exhibits a robustness to error much like the Cox method, but offers a significant advantage in terms of application for real-time analysis. We begin by demonstrating the results of a feasibility study of the method applied to synthetic data where there is significant model error, followed by application to the *in vitro* neural culture network.

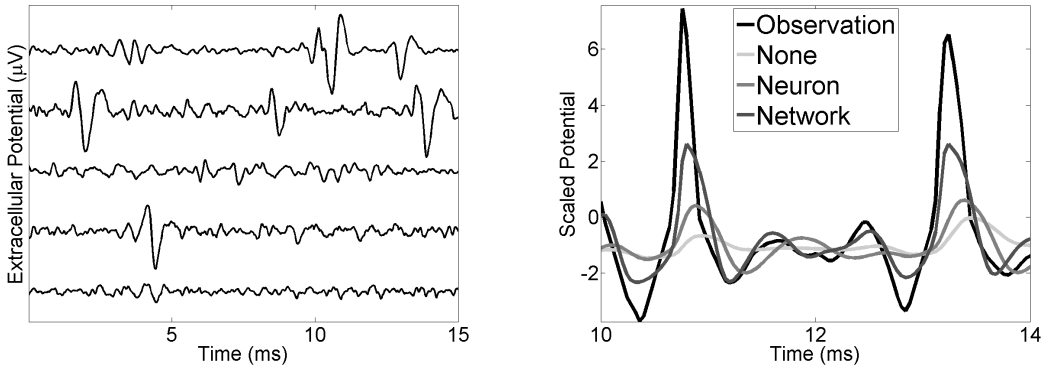

Figure 6.1: (a) Small section of recorded extracellular potential *in vitro* (five traces shown). Sample neural spike waveforms from the MEA differ in shape from generic neuron models, which simulate intracellular currents. (b) Three assimilation results for top trace in (a). Observation (black) consists of preprocessed (see text) extracellular waveform compared with its intracellular model counterpart. When no parameters of the model are fit (marked None, light grey) the observation cannot track successfully. By fitting individual neuron parameters (marked Neuron, medium grey) more of the observation is tracked. When the full network parameters are fit in addition to the neuron parameters (marked Network, dark grey), the observation is fairly effectively tracked, showing the importance of including the network structure in assimilation.

6.1 Nonlinear Data Assimilation for Link Tracking

For assimilation purposes, we posit a general nonlinear system with an n-dimensional state vector x and m-dimensional observation vector y evolving according to

$$\begin{aligned} x_{k+1} &= f(x_k, t_k) + w_k \\ y_k &= h(x_k, t_k) + v_k \end{aligned} \tag{6.1}$$

where w_k and v_k are Gaussian noise terms with covariance matrices Q and R respectively.

For our purposes, f in (6.1) is chosen to be a generic spiking model. We used the

Hindmarsh-Rose intracellular model [20] parametrized as in [80]:

$$\begin{aligned}
\dot{V}_i &= a_i V_i^2 - V_i^3 - y_i - z_i + I_i + \sum_{j \neq i}^{n} \Gamma_{\mathrm{HR}}(V_j) V_j + \sigma \dot{W}_{Vi} \\
\dot{y}_i &= (a_i + \alpha_i) V_i^2 - y_i + \sigma \dot{W}_{yi} \\
\dot{z}_i &= \mu_i (b_i V_i + c_i - z_i) + \sigma \dot{W}_{zi}
\end{aligned} \tag{6.2}$$

for $i = 1 \ldots n$, and where $\Gamma_{\mathrm{HR}}(V_j) = \beta_{ij}/(1 + 9e^{-10V_j})$ is a gating function that regulates the amount of input between neurons. Here V is the membrane variable, y (resp., z) represents the fast (resp., slow) channel dynamics, I is the input current and a, b, c, α, μ are model parameters whose values determine the different spiking behaviors of the neuron such as tonic spiking or bursting. The parameters β_{ij} represent the connectivity parameter from neural assembly j to neural assembly i, and $\dot{W}$ represents uncorrelated white noise of unit variance. The only observable used by the data assimilation procedure is the membrane voltage $h(V, y, z) = V$.

The choice of gating function $\Gamma_{\mathrm{HR}}(V_j)$ is used to force the model parameters to be fit from the spiking dynamics of the measured data, in addition to physiological plausibility. This is based on a hypothesis that information is passed in a neural network primarily through spiking behavior, and we strive to avoid spurious fitting of model parameters from arbitrary resting potentials between spikes. We found through computer experiments with synthetic data that in the absence of a gating function the model parameters are easily fit from resting data, which overemphasizes the confidence in parameter fitting.

As discussed in Chapter 5, we can treat the l-dimensional parameter vector p as extra states of the model, with trivial dynamics. The augmented state vector, consisting of the original n model states and l parameters, is estimated by the EnKF. Fig. 1(b) compares the reconstruction of the observable by the EnKF in three scenarios: with (1) fitting only the n state variables (no parameters), (2) the state variables plus model parameters α_i, a_i,

and I_i, and (3) the state, model and network parameters β_{ij}.

The extracellular waveform shown in Fig. 1 was recorded from a network of cultured mammalian spinal cord neurons plated onto an MEA as described in Chapter 2. Fig. 1(a) shows several time traces of the recorded potential at separate electrodes.

Since the recorded extracellular potential waveform differs from the Hindmarsh-Rose waveform, preprocessing is required. We connected the recorded potential to its intracellular counterpart through the relationship $dI/dt \approx E$ where E is the recorded extracellular potential and I is the intracellular potential [81]. The integration required was done using a simple moving average algorithm. The resulting approximation was then scaled as necessary to ensure stability when assimilated to our general model.

The design of the MEA allows for the possibility of multiple unit recordings at each electrode, although in the case reported here, offline analysis of the active electrodes showed single unit activity at each electrode. In a real-time analysis of network structure, sorting of individual units may not be feasible. Each electrode can thus be considered as a neural assembly, or population response, and subsequently be modeled as such. On the other hand, if analysis is to be done offline then units can be distinguished, for example, through principal component analysis (PCA) and use of a clustering algorithm.

The Hindmarsh-Rose equations were chosen for this problem since they can represent a significant range of neuronal behavior with only three dynamical variables. To resolve the possible error in estimated connectivity caused by unmodeled neuronal dynamics, some of the model parameters are left as free states to be estimated along with the model variables and connection parameters. These additional parameters give the EnKF extra degrees of freedom to resolve the model error and aid in the assimilation process. While there are more biophysically accurate models in the literature, the consequence of using these models is a more demanding estimation problem caused by the increase in variables and parameters. Our interest is in having a faithful representation of network connectivity, making this additional complexity unnecessary.

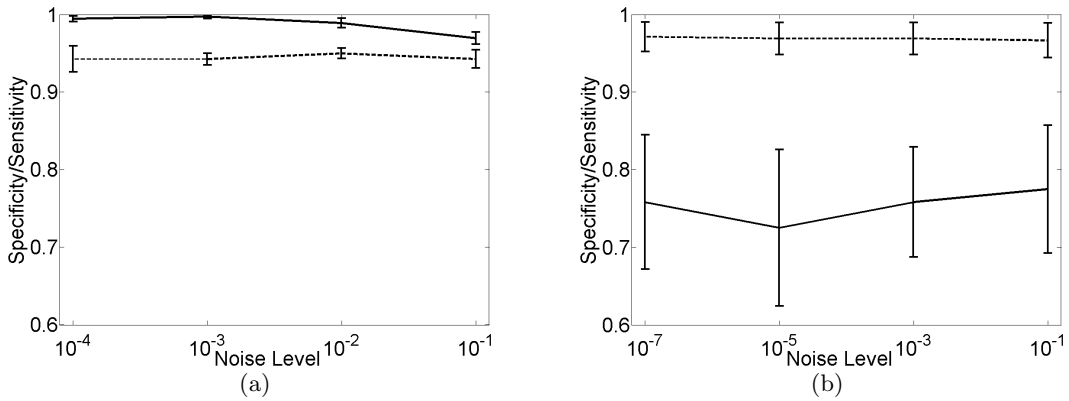

Figure 6.2: Specificity (dotted line) and sensitivity (solid line) results of our method's identification of network links at the 95% confidence level when model error caused by noise is considered. Networks consist of (a) 10 Hindmarsh-Rose neurons (b) 5 Hodgkin-Huxley neurons with 40% network connectivity. In both cases, Hindmarsh-Rose was the EnKF network model. Error bars represent standard error over 10 network realizations of length 8 sec. Identified links are those whose estimated β connectivity parameter is greater than two times their filter-estimated standard deviation.

6.2 Statistical Identification of Network Links

The connectivity strength between neural assemblies will be represented by a parameter vector $\boldsymbol{\beta}$, where β_{ij} indicates the connection parameter from neural assembly j to neural assembly i. Our goal is to use the recorded time series from each electrode to continuously estimate these β_{ij} parameters and determine which of the estimates are statistically significant, resulting in identified network links.

Using the ensemble Kalman filter produces an estimate of the error of the parameter estimate, given by the diagonal entry of the covariance matrix P_k^+ corresponding to the parameter in question. Let β_{ij} be an estimated parameter in the state vector at time step k and let σ^2 be the corresponding diagonal entry of the covariance matrix P_k^+. The standard confidence interval for β_{ij} with confidence level γ_0 is $\left[\beta - \kappa_{(1-\gamma_0)/2}\sigma, \beta + \kappa_{(1-\gamma_0)/2}\sigma\right]$ where $\kappa_{(1-\gamma_0)/2}$ is the $(1-\gamma_0)/2$ quantile of the normal distribution. Thus, we can apply a Wald test for connectivity parameter $\beta_{ij} = 0$ by asking whether 0 lies in the above confidence interval.

Fig. 6.2(a) shows that when data is fit with the correct model, the specificity and sensitivity results are correct at the 95% confidence level, independent of system noise. Here we used the Hindmarsh-Rose equations (6.2) both to generate data and as f in the EnKF equations.

To validate the method for use with real data, in Fig. 6.2(b)we test significant model error, caused by a mismatch in dynamics. Consider the Hodgkin-Huxley model [15] with original parameters as implemented by [82], expanded to a network of n equations

$$\begin{aligned}
\dot{V}_i &= -g_{Na}m^3h(V_i - E_{Na}) - g_K n^4(V_i - E_K) - g_L(V_i - E_L) + I + \sum_{j\neq i}^{n} \Gamma_{\mathrm{HH}}(V_j)V_j \\
\dot{m}_i &= a_m(V_i)(1 - m_i) - b_m(V_i)m_i \\
\dot{h}_i &= a_h(V_i)(1 - h_i) - b_h(V_i)h_i \\
\dot{n}_i &= a_n(V_i)(1 - n_i) - b_n(V_i)n_i
\end{aligned}$$

with model functions

$$\begin{aligned}
a_m(V) &= 0.1(V + 40)/(1 - \exp(-(V + 40)/10)) \\
b_m(V) &= 4\exp(-(V + 65)/18) \\
a_h(V) &= 0.07\exp(-(V + 65)/20) \\
b_h(V) &= 1/(1 + \exp(-(V + 35)/10)) \\
a_n(V) &= 0.01(V + 55)/(1 - \exp(-(V + 55)/10)) \\
b_n(V) &= 0.125\exp(-(V + 65)/80)
\end{aligned}$$

for $i = 1, \ldots, n$ and with gating function $\Gamma_{\mathrm{HH}}(V_j) = \beta_{ij}/(1+e^{-10(V_j+40)})$ connecting neurons as in (6.2). The observables are the voltage variables V_i perturbed with noise, namely $V_i + \sigma\dot{W}_i$. We assimilate this Hodgkin-Huxley data to the Hindmarsh-Rose model (6.2) and use the EnKF method to estimate the connectivity parameters.

The identification of network links using data from a significantly different neuron model presents a new challenge. To handle the increased model error, we designate certain of the model parameters as free states while fixing others. We fix $b = 9, c = 5, \mu = .001$ and leave a, α, I as free states to be estimated along with the model variables. Additionally, we have to carefully tune parameters in the EnKF algorithm to prevent the covariance matrix from becoming degenerate and causing filter divergence, using a covariance inflation method. See [30] and the references therein for approaches to covariance inflation and tuning.

In an attempt to develop a fair test for our method, we simulate random networks of five noisy Hodgkin-Huxley neurons where each connected pair has a bi-directional relationship. That is, for every β_{ij} there is a β_{ji} in the network. Observational noise is used on the horizontal axis rather than system noise since the discrepancy in dynamics between the Hodgkin-Huxley data and our neuron model is already so large that the addition of extra system noise has no important effect.

Fig. 6.2(b) shows that the EnKF method is successful in determining the neurons that are connected to one another, identifying that a statistically significant connection exists between a connected pair. As the amount of observational noise increases, our method maintains specificity around 95% showing that our results are statistically significant. Sensitivity persists around 70% showing that the method is finding the majority of the network links.

6.3 Link Tracking

A significant application of this method is to detect the appearance and disappearance of connections in nonstationary networks, such as neural cultures. To verify the methodology for this purpose, we ran a simulated test of a Hodgkin-Huxley neural network where one of the network connections β_{ij} was turned on and off randomly. We used the above method to assimilate the voltage measurements only from the network, and purposely used the wrong model (Hindmarsh-Rose) in the EnKF, so that model mismatch was severe, and asked the method to track the changes.

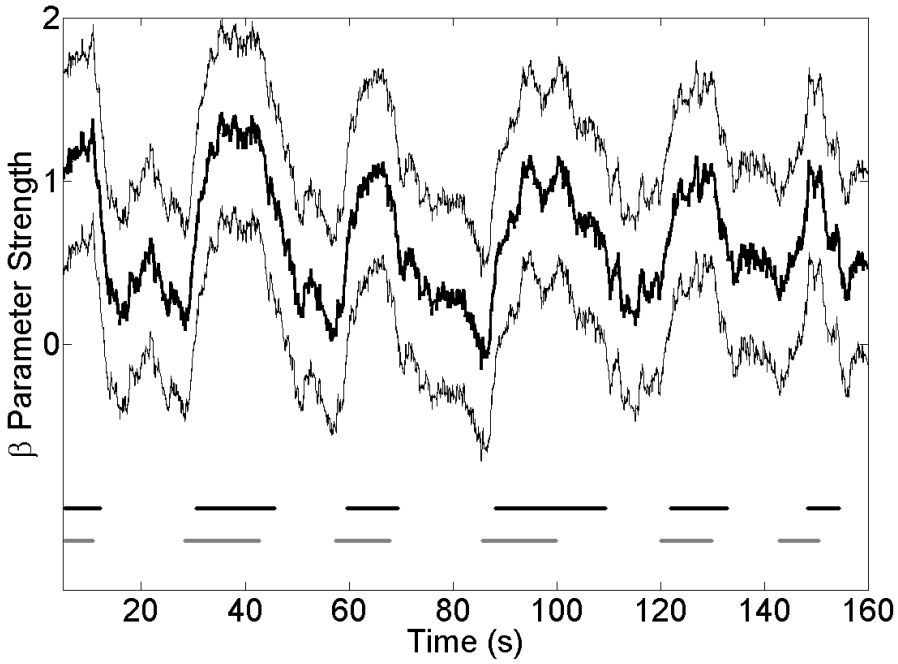

Figure 6.3: Tracking results of a time-varying connection in a five neuron network of Hodgkin-Huxley neurons over 160 seconds of simulation data. Connection turned on/off randomly. Bottom traces of figure show the actual "on" time (grey bar) and the filter-estimated "on" time of the connection (black bar). Top traces of figure show the filter estimated connection strength and corresponding 95% confidence region.

We established the following protocol for determining the on/off transitions of the connection. When the connection is off, the protocol says to declare a transition from "off" to "on" when the mean estimated connection strength increases beyond the minimum (since the last "on" transition) of the confidence interval maximum; and vice versa for "off". Fig. 6.3 shows the ability of the method to detect these changes with minimal latency. The reconstructed parameter value of the β_{ij} as a function of time is plotted in the upper trace, along with 95% confidence limits. The lower grey trace is the imposed "on" time of the connection; in between these times the connection is set to zero. The lower black traces show the intervals at which the assimilation method finds a nonzero connection according to the above protocol. These results show the ability of the method to detect nonstationarities with minimal latency.

In Fig. 6.4, we apply the method to the *in vitro* data from the cell culture. Each panel of the figure shows the method's continuous tracking of a different β_{ij} connectivity parameter with the appropriate 95% shaded confidence region over 160 seconds of recorded data. A connection is detected with 95% confidence when the 95% confidence region does not include 0. Panels (a)-(c) show three estimated β_{ij} parameters and their respective confidence regions from a small network with five active electrodes. (a) and (b) show identified links within the confidence level, while panel (c) shows a clear non-connection. Panel (d) shows a β_{ij} parameter from a larger network with twelve active electrodes. Here is a difficult case. As the filter gains more information about the network, it is stating that the connection exists, at least within the confidence level used.

Fig. 6.5(a) shows the estimated network connection matrix and corresponding time of statistical significance for 160 seconds of data from the small MEA network with five active electrodes at the 95% confidence level. Of the twenty possible connections in this network, only seven were determined to be statistically significant. These were found significant throughout the entire data series showing that our method was highly confident in their existence.

Fig. 6.5(b) shows the estimated connection matrix computed from a 160 second interval of data from the larger network with twelve active electrodes at the 95% confidence level. Out of the possible 132 connections, 28 were found to be significant at some time during the interval. This larger network presented questionable cases, typically whereby a connection parameter was initially not significant but became an identified link as more data was assimilated. All of the 28 connections that were statistically significant for part of the interval were significant for at least 50% of the interval, and 14 of the 28 were significant during more than 90% of the interval, as shown in the figure.

6.4 Conclusion

A method that can carry out sequential tracking of neuronal network links has a major advantage for experimental purposes. Using an EnKF with a general neuron model is a way to provide a statistically driven estimate of network connectivity that is updated continuously as data arrives, unlike offline methods such as [77–79]. This allows application to network structures with moderate nonstationarity, a typical feature of neural ensembles and biological networks in general. As shown above, this algorithm for detecting connectivity meets our criteria of being statistically based, robust to error and capable of real-time implementation.

We showed in simulation and with measured data from neural cultures that such a method can work successfully. The choice of the model in the EnKF plays a critical role. Figs. 2 and 3 illustrate the dependence on model mismatch. Certainly, if the model is not representative of the basic dynamics of the underlying system, results will be compromised. A feature of this approach is that allowing parameters of the mathematical model in the EnKF to float may temper the mismatch between the dynamics of the model and the experimental system, resulting in more accuracy in the fitted connection parameters. A deeper study of the dependence on models is a fruitful direction for future work.

A related question is whether nonstationarity of the underlying system can confound attempts to find the correct connections. Undoubtedly this is true in some circumstances; in particular, the connections may be changing during the experiment. We attempt to minimize false conclusions by allowing parameters in the model to drift along with the data, to possibly correct for some of the nonstationarity in the experimental system, independent of the connections, but careful analysis of this possibility is beyond the scope of this work.

While the MEAs are plated at a high density of neuronal cells, observation of the network is restricted to the array's 64 electrodes. While this may seem an undersampling of the network, tracking the connections between observed neural ensembles at each electrode may allow us to implement significant network control. This new technique opens up several possible experimental strategies, including pharmacological and electrophysiological studies

where the effects of an applied drug or pulse pattern on connectivity are to be determined. The ability to continuously track connectivity is designed to provide real-time feedback in an experimental situation, allowing an researcher to adjust observation, control or other interventions.

Although we expect the statistical method outlined here to greatly expedite several proximate research goals such as tracking and control of neural cultures, the further objective of generalizing the application of this statistical method from cultures to the *in vivo* brain presents clear challenges. While the cultures present dynamics that are on the whole relatively non-synchronous, activity arising from giant depolarizing potentials [83] and sharp wave ripple events [84] show significant synchronicity, even in heterogeneous populations of cells. Extreme activity of this type could make network connectivity an unobservable quantity, due to the swamping of evidence necessary to determine cause-and-effect. In such cases, the method outlined here could be prevented from providing a reliable estimate of the link structure as long as the synchronization persisted. Further development of the method described here or complementary approaches for determining connectivity in these and other complex biological events is the subject of future work. Though these limitations exist, implementation of our method in *in vivo* experimental situations such as those described in [85] and [86] could provide valuable insight to researchers.

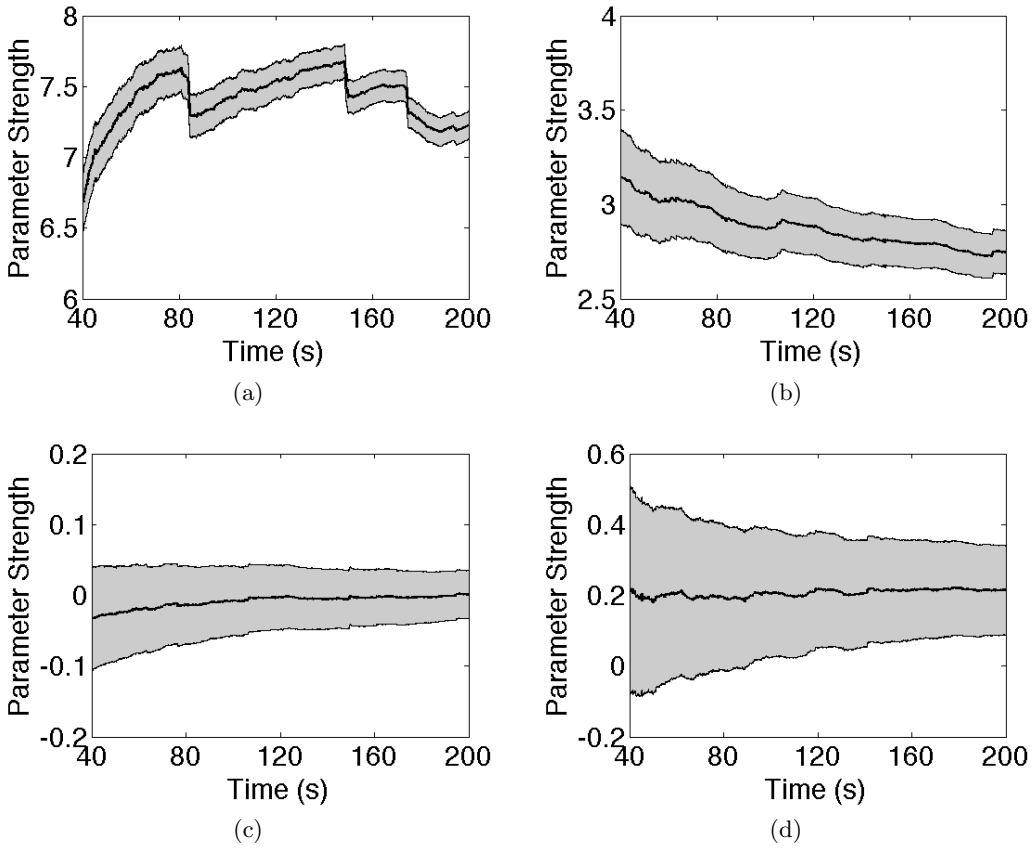

Figure 6.4: Four example in vitro β_{ij} parameters tracked over 160 seconds of data. Solid black line indicates the estimated connection strength and shaded grey area denotes 95% confidence region. A link is detected with 95% confidence when the 95% confidence region does not include 0. Panels (a)-(c) show three estimated β_{ij} parameters from a small network with five active electrodes, (a) β_{41} (b) β_{35} (c) β_{15}. (a) and (b) show identified links within the confidence level and panel (c) shows a non-connection. Panel (d) shows a difficult case from the larger network with twelve active electrodes. Initially the connection β_{53} is not significant, but as the filter gains more information about the network it becomes an identified link.

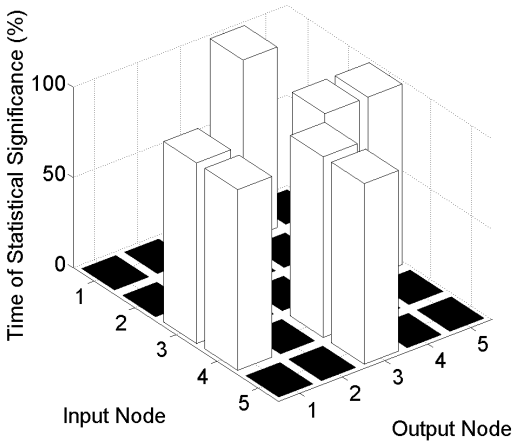

(a)

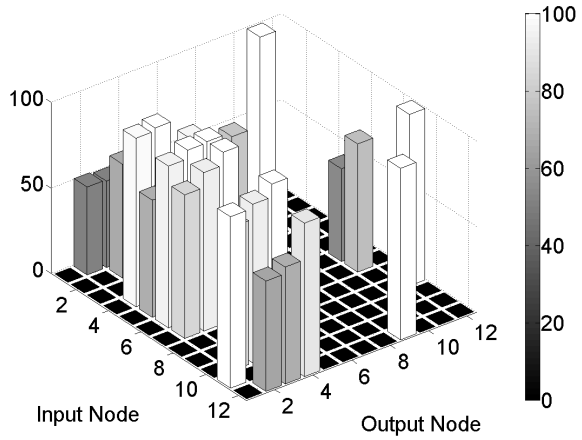

(b)

Figure 6.5: Estimated network connection matrices for 160 seconds of data from two MEA networks. The percentage time of statistical significance for (a) smaller network with five active electrodes and (b) larger network with twelve active electrodes is shown. A β_{ij} connection was determined to be significant by our method when its 95% confidence region did not include 0. In (a), seven of twenty possible connections were found to be significant throughout the entire data set. In (b), 28 of 132 possible connections were found to be significant for at least 50% of the time interval.

Chapter 7: Reconstructing neural dynamics using data assimilation with multiple models

The following chapter has been published here [87].

The standard data assimilation technique is limited to the reconstruction of state variables and parameters that are explicitly represented in the model. In this chapter, we show how this general methodology can be naturally extended further, to reconstruct variables of the system that do not appear in the model, but for which limited time series measurements are available. A result of Takens [88–91] shows that sufficiently generic time series measurements can be used to reconstruct system dynamics. This knowledge has been long used as a basis for black-box prediction, noise reduction, and control protocols for nonlinear systems. Here we take a first step at merging this powerful theory with modern methods of data analysis that can exploit information from models.

The basic concept involves assimilating the available time series in parallel with multiple, different versions of the model. In our examples, we use a single model under a variety of fixed parameter settings. During a training period, data from both modeled variables and the unmodeled variable are available, and a parameterized combination of reconstructed model variables is fit to the unmodeled variable. After the training period, this combination is used to track the unmodeled variable. An arbitrary number of unmodeled variables can be tracked simultaneously and independently with this method.

Our approach essentially merges two lines of research on modeling and predicting behavior of nonlinear systems. One direction, motivated by the seminal paper by Lorenz [92], attempts to build a collection of models with slightly different parameters, and regress during a training period on the outputs of the models of a particular variable to build a good predictor for that variable [93, 94]. Independently, researchers in data assimilation have

used multimodel versions of the Kalman filter [95] and the EnKF [96–98] to improve the tracking capability of the modeled variables. Our approach combines the ideas by training a multimodel EnKF on some known time series data from a variable that is not included in the underlying model, and using the fitted result to predict the unmodeled variable after the training period ends. We think of the approach as a "platypus" method, since our basic ansatz is that the unmodeled variable is a combination of nominally unrelated parts.

A further advantage of a data assimilation approach to the problem is that after the training period, the unmodeled variable can be computed in real time. Moreover, if further training data becomes subsequently available, it can be easily exploited to further refine the parameterized combination, or to do realtime tracking under circumstances of drifting parameters.

7.1 Reconstructing Unmodeled Variables

To illustrate the idea, assume the system model

$$\begin{aligned} \dot{x} &= f(x,p) + \omega_t \\ y &= h(x) + \nu_t \end{aligned} \tag{7.1}$$

for state vector x and vector p of parameters. Here ω_t and ν_t are white noise inputs. The function h is a vector-valued observation of the state. The standard filtering problem is to use the time series of observations y_t to calculate an estimate for the current state x.

The innovation of this method is to go beyond estimating unobserved variables and parameters in the model, i.e. the components of x and p, to estimate quantities that are not explicit model variables or parameters. We assume that a time series S_t of the desired unmodeled variable is available during a training phase, with the goal of continuing to estimate the variable after the training period has ended.

We construct a parallel set of m subfilters, each of which are the system model with separate parameter settings p_i. This parallel set is used for data assimilation during the

training phase, corresponding to the equation

$$\begin{aligned} \dot{w} &= F(w) + \omega_t \\ \begin{bmatrix} y \\ \vdots \\ y \\ S \end{bmatrix} &= H(w) + \nu_t \end{aligned} \tag{7.2}$$

where

$$w = \begin{bmatrix} x^1 \\ \vdots \\ x^m \\ c^1 \\ \vdots \\ c^m \\ d \end{bmatrix} \quad F = \begin{bmatrix} f(x, p_1) \\ \vdots \\ f(x, p_m) \\ 0 \\ \vdots \\ 0 \\ 0 \end{bmatrix} \quad H(w) = \begin{bmatrix} h(x^1) \\ \vdots \\ h(x^m) \\ \sum_{i,j} c_j^i x_j^i + d \end{bmatrix}$$

Note that each x^i denotes a separate copy of the system state vector, with n components x_j^i for $j = 1, \ldots, n$. Each c^i is an unknown coefficient vector of n components c_j^i that will be learned along with the states x^i during the assimilation process, in order to best fit the unmodeled variable $S = \sum_{i,j} c_j^i x_j^i + d$. The inputs to the assimilation procedure during the training phase are the modeled observables y_t, and the time series S_t of the unmodeled variable, that is provided only during the training phase. The coefficients c_j^i and d are estimated during the training phase (along with the system variables x_j^i), and then fixed

during the *prediction phase*, which uses only the y_t inputs, and assimilates the system model

$$\begin{aligned} \dot{w} &= F(w) \\ \begin{bmatrix} y \\ \vdots \\ y \end{bmatrix} &= H(w) \end{aligned} \tag{7.3}$$

where

$$w = \begin{bmatrix} x^1 \\ \vdots \\ x^m \end{bmatrix}, F = \begin{bmatrix} f(x, p_1) \\ \vdots \\ f(x, p_m) \end{bmatrix}, H(w) = \begin{bmatrix} h(x^1) \\ \vdots \\ h(x^m) \end{bmatrix}.$$

During the prediction phase, the expression $\sum_{i,j} c_j^i x_j^i + d$ gives an estimate of the unmodeled quantity S using only the y_t inputs.

As a simple demonstration, we describe the reconstruction of a gating variable from the Hodgkin-Huxley (HH) neural model [15] consisting of four differential equations, modeling the voltage V and three gating variables h, m and n (see Chapter 6). We will use the Hodgkin-Huxley equations to generate a time series of the four variables. However, for the purposes of the illustration, we make no use of the knowledge of how the time series was created. As the assimilation model, we purposely choose an unrelated, standard spiking model, the Hindmarsh-Rose (HR) equations [20]

$$\begin{aligned} \dot{V} &= y - V^3 + 3V^2 - z + I \\ \dot{y} &= 1 - bV^2 - y \\ \dot{z} &= \tau(s(V + 1) - z) \end{aligned} \tag{7.4}$$

where V represents voltage, y is a fast recovery variable and z is a slow variable. The

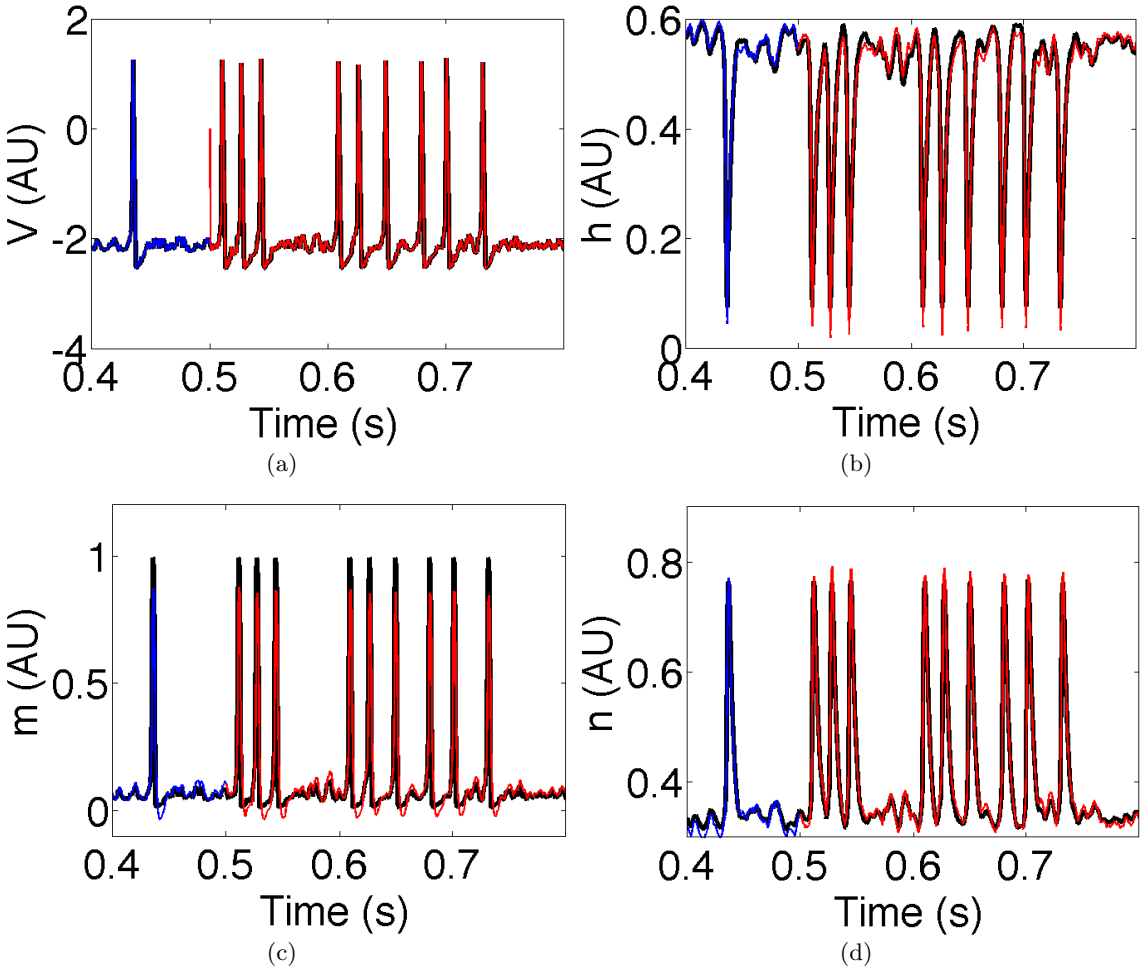

Figure 7.1: Hodgkin-Huxley time series is input into the EnKF using Hindmarsh-Rose multiple models. The end of the training phase and beginning of prediction phase are shown. (a) Hodgkin-Huxley voltage (black) and assimilated version of voltage in training phase (blue) and prediction phase (red). (b) Hodgkin-Huxley gating variable h (black) and assimilated version of h. During the prediction phase (red), only the Hodgkin-Huxley voltage is available to the EnKF. The procedure also obtains the other two Hodgkin-Huxley gating variables, (c) m and (d) n.

rate of z is controlled by time scale parameter τ, while I, b and s are free parameters to be estimated alongside the state variables V, y and z by the EnKF [31, 50, 61, 62]. We use $V(t)$ and $h(t)$ from the Hodgkin-Huxley series during the training phase. Note that (1) the gating variable $h(t)$ is not explicitly represented as a variable in the assimilation model (the

Hindmarsh-Rose equations) and is therefore an unmodeled dynamic, and (2) the waveforms of HR (see Fig. 2(b) for an example) are quite unlike all waveforms of the HH variables (see Fig. 1(a)-(d)).

In the assimilation process, we use two HR models to reconstruct $h(t)$, with timescale parameters $\tau_1 = 0.001$ and $\tau_2 = 0.1$, respectively. According to (7.2), we make the approximation $h(t) \approx \sum_{i,j} c_j^i x_j^i + d$. Using two assimilation models, this approximation during the training phase can be achieved several ways. If we reconstruct using only the y variables from the models, we find $h(t) \approx -2.46y_1 + 1.92y_2 + 0.50$ as a result of the training phase. This approximation gives us prediction root mean squared error (RMSE) = 0.140. A much improved reconstruction uses only the z variables, giving the approximation $h(t) \approx 1.21z_1 - 0.17z_2 - 1.35$ which yields prediction RMSE = 0.025. Using both the y and z variables yields the most accurate estimate $h(t) \approx -0.42y_1 + 0.33z_1 + 0.48y_2 - 0.16z_2 - 0.83$, and prediction RMSE = 0.016, shown in Fig. 1(b). When it is unknown *a priori* which variables allow for a more faithful reconstruction of the unmodeled quantity, all variables can be considered for discovery of the optimal weighting. We repeat this process and reconstruct the $m(t)$ and $n(t)$ gating variables, shown in Fig. 1(c-d), using two assimilation models each.

7.2 Reconstructing Seizure Dynamics

To further simulate the type of model error we would encounter in a laboratory setting, we consider data generated from a second, more sophisticated system as described in [16], where it was used to investigate ionically mediated bursting. The model equations (see Appendix B2) include the membrane potential based on transmembrane currents for sodium and potassium. The gating variables for potassium activation and sodium inactivation are modeled dynamically whereas the sodium activation is assumed instantaneous. In addition, the ionic dynamics for extracellular and intracellular potassium and sodium concentrations,

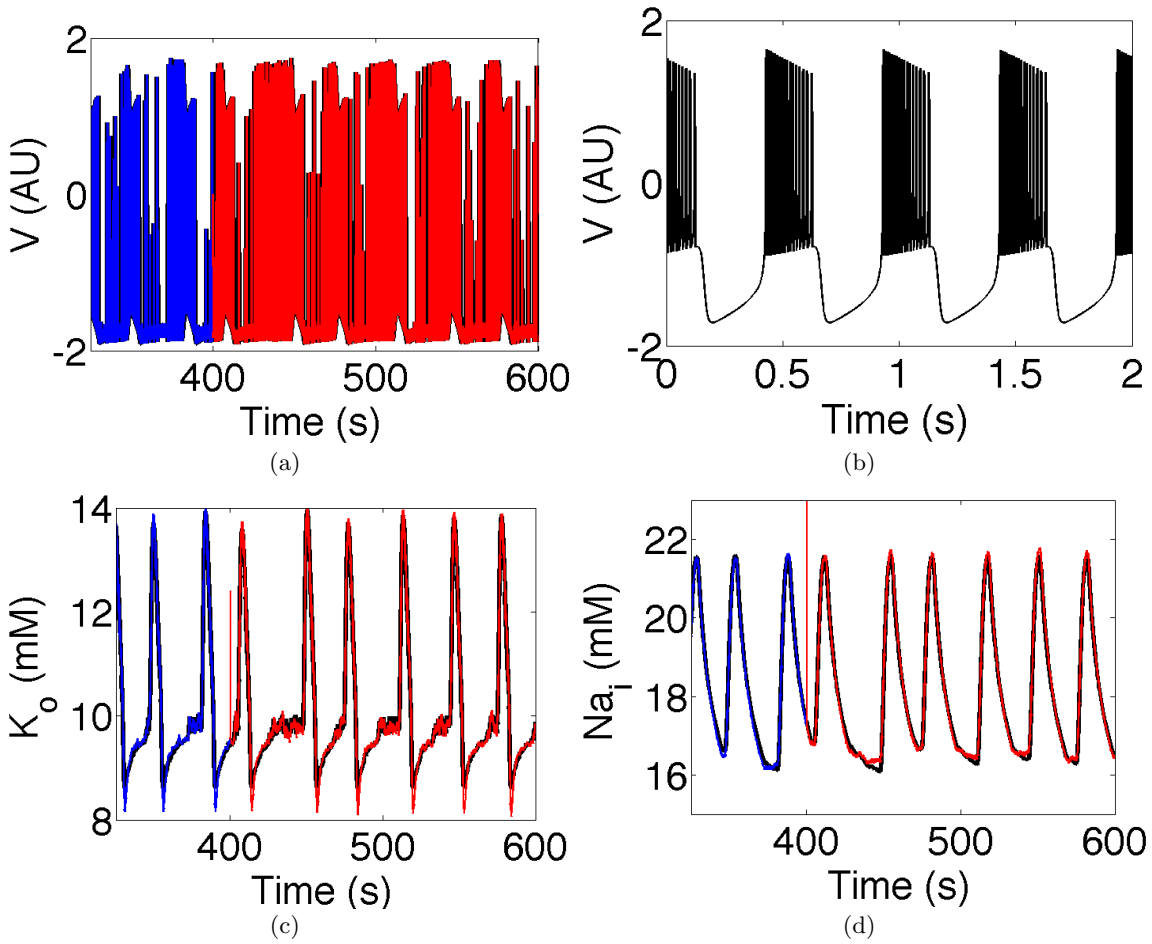

Figure 7.2: A single seizing neuron is driven by a Poisson spike train with constant parameter λ. The neuron voltage (a) is continuously measured, and assimilated using the EnKF with three versions of HR, whose voltage trace is shown in (b) with parameters $b = 5, \tau = 0.001, s = 4$ and $I = 0$. Potassium (c) and sodium (d) are only observed for a brief training period of 200 s. During the training period, our algorithm finds the optimal combination of the model variables (blue). After this training period, we can predict (red) the potassium (RMSE = 0.12) and sodium (RMSE = 0.11) dynamics from the three HR models.

respectively, are modeled by two equations. Sodium concentrations depend only on transmembrane conductances making their intra- and extracellular concentrations linked through mass conservation. The extracellular potassium dynamics also include glial buffering.

The model was driven by a Poisson spike train to create a sequence of irregular seizures, shown in Fig. 2(a). As with the HH data from our first example, the potential is treated

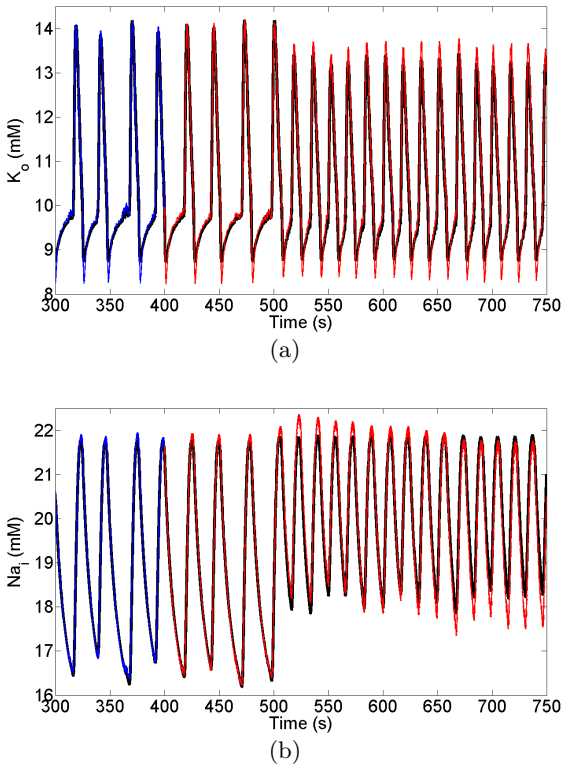

Figure 7.3: A single seizing neuron is driven by a poisson spike train with increasing time-varying poisson parameter λ. Three models are used for the data assimilation. The neuron voltage (a) is continuously measured while the potassium (b) and sodium (c) are only observed for a brief training period of 200 s. After the training period during which we find the optimal combination of the models (blue), the measurement of potassium and sodium is turned off and we predict (red) their changes while only assimilating the neuron voltage. Our prediction of potassium and sodium both prove to be fairly robust to the nonstationarity of the driving input (RMSE = 0.18 and RMSE = 0.27 respectively). There is some additional prediction error caused by the variability in seizure rate, but overall the correct dynamics are predicted.

as the observable of the system. The goal is to use data assimilation with the (unrelated) HR model to reconstruct and predict the sodium and potassium concentrations, given only the voltage and a brief sequence of training data. The increased complexity of these data requires us to use three copies of the HR model. We set two of the models to have timescale parameters $\tau_1 = 0.001$ and $\tau_2 = 0.0001$ and individually optimize the third timescale, τ_3, for minimum training phase RMSE. Fig. 7.2 shows the resulting reconstruction of the

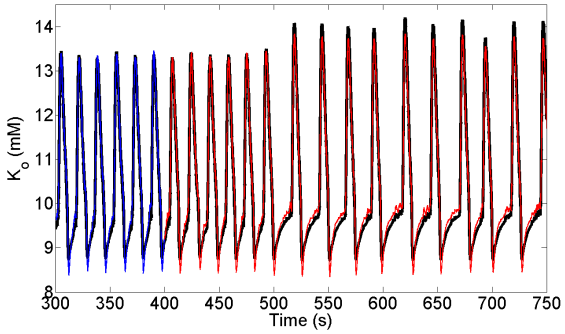

(a)

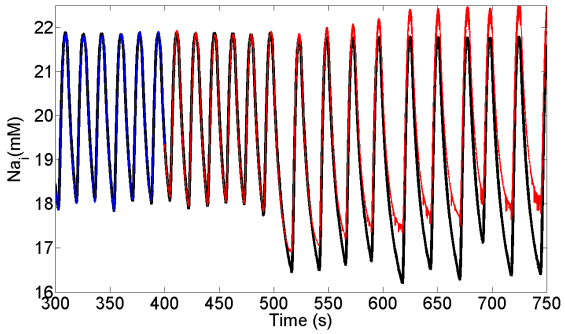

(b)

Figure 7.4: A single seizing neuron is driven by a poisson spike train with decreasing time-varying poisson parameter λ. Three models are used for the data assimilation. The neuron voltage (a) is continuously measured while the potassium (b) and sodium (c) are only observed for a brief training period of 200 s. After the training period during which we find the optimal combination of the models (blue), the measurement of potassium and sodium is turned off and we predict (red) their changes while only assimilating the neuron voltage. Once again, the prediction of potassium is fairly successful (RMSE = 0.18). However, in this instance we can see that our prediction of sodium suffers significantly (RMSE = 0.64). This additional error could be resolved by expanding the training data set or through periodic measurements of the concentrations allowing us to adjust the optimal model combination.

potassium and sodium dynamics from this system. Using only three assimilation models we are able to reconstruct these quantities with a high degree of accuracy (RMSE = 0.12 and 0.11, respectively).

To demonstrate the ability of our method to reconstruct unmodeled variables under system nonstationarity, we varied the rate of the stimulating Poisson spike train. Figure 7.3 shows the potassium and sodium reconstruction results when the rate decreases and Figure

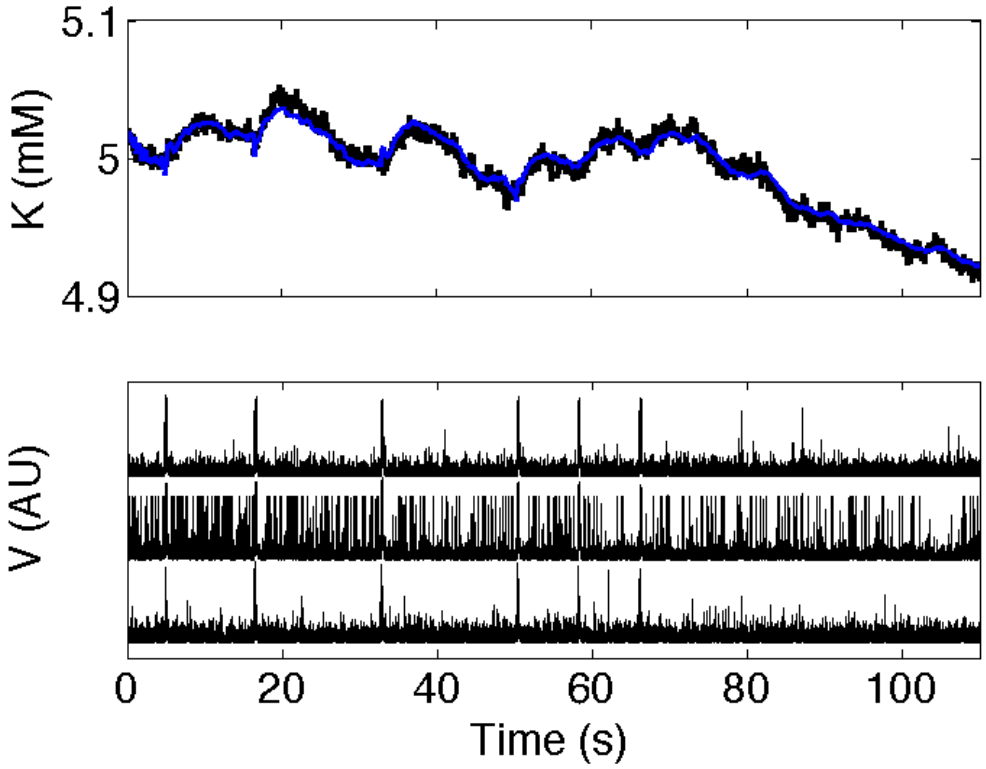

Figure 7.5: A potassium sensitive electrode is used to record the extracellular potassium concentration changes in a small region between three active electrodes of an *in vitro* cortical culture plated on an MEA. During a 110 s training period, the potential from the three electrodes is assimilated and estimated with our EnKF (bottom) while an optimal combination of the model variables is found (top, blue) to reconstruct the measured potassium (top, black). For this example, each electrode is represented by four differently parameterized models, resulting in a total of twelve system models.

7.4 shows the reconstruction when the rate increases. While the predictive capabilities of our reconstruction proves accurate under some system nonstationarity, the degradation in accuracy of the sodium reconstruction in Figure 7.4 suggests that periodic measurements or an extended training data set would be needed in some situations.

7.3 Tracking *In Vitro* Extracellular Potassium

To apply the method in a laboratory setting, we collected a potassium time series from a neural culture experiment. Neural cultures were prepared as discussed in Chapter 2. Each

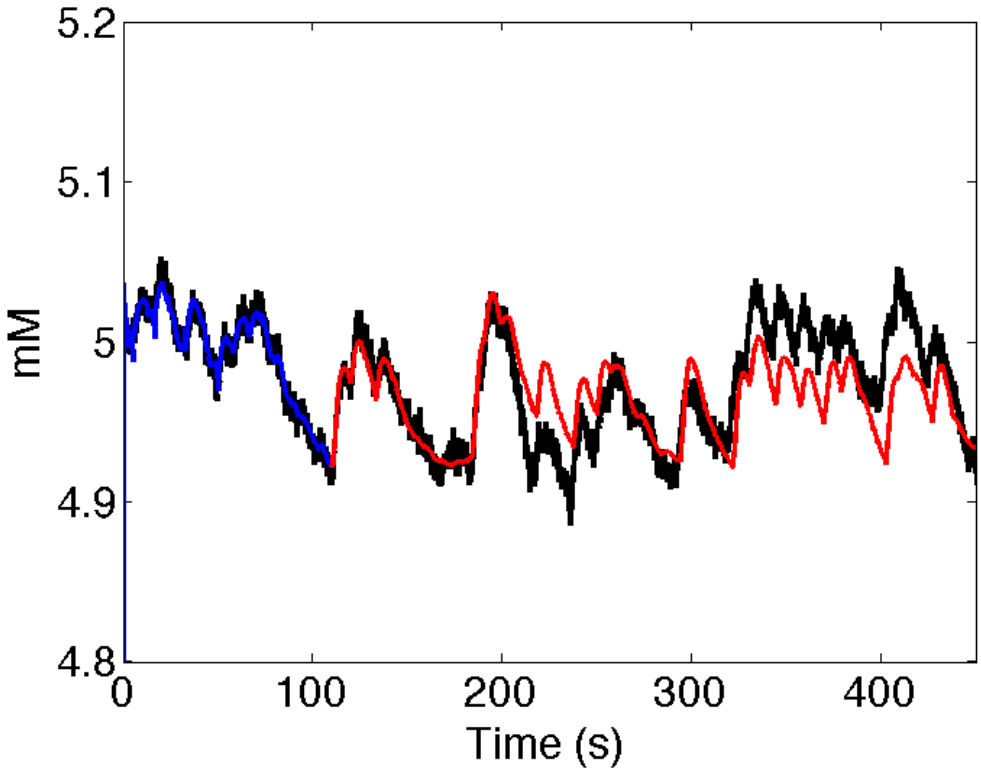

Figure 7.6: After the training period is complete, eqn. (7.3) accurately predicts (RMSE = 0.024) the potassium concentration changes during spontaneous activity while using as input only the neural potential from 3 MEA electrodes.

electrode was recorded at a rate of 25 kHz, but here was downsampled to 1 kHz. Individual units on active electrodes were not sorted, meaning each electrode was considered as a neural assembly. The recorded time series from each electrode was filtered and rectified prior to assimilation.

Local potassium measurements were performed using the same type of resin-based potassium sensitive microelectrodes used in slice experiments [99]. Potassium and reference electrodes are positioned in the mat of cultured cells located in the vicinity of a three active MEA recording sites. The potassium data are acquired using an high impedance differential amplifier and digitized and recorded at 100 Hz. The data are low-pass filtered and input to the Nernst equation to find to potassium concentration in the vicinity of the electrode.

Fig. 3 shows the recorded *in vitro* neural activity from each of the three electrodes during the training phase. The assimilation is done with eqn. (7.2) using four HR models for each electrode, with timescales $\tau_1 = 0.001, \tau_2 = 0.0001, \tau_3 = 0.005, \tau_4 = 0.0005$, resulting in a total of twelve system models. Here the training period is only 110 seconds, during which the potassium and potential are available for assimilation and an optimal weighting of the twelve models is found to reconstruct the potassium time series. Fig. 4 shows the prediction phase, where we are able to track the potassium dynamics while only assimilating the neural potential. Discrepancy between the actual and predicted values may be partially attributed to uncertainties in our measurement, since the potassium is recorded from a general region rather than a specific cell and there are likely other active neurons in the area, contributing to the potassium changes whose potential we are unable to capture due to the MEA architecture.

7.4 Conclusion

We have introduced an extension of standard data assimilation techniques, based on Takens' embedding theorem, that uses a short time series from an unmodeled variable to train a predictor for the variable using multiple versions of the model. The use of multiple versions serves to bring the strength of relatively simple mathematical modeling to bear on complicated dynamics, by training with time series data. For simplicity, we described an implementation with the Ensemble Kalman Filter, and used the Hindmarsh-Rose as a basic model, even though the latter is designed for intracellular, not extracellular dynamics. With appropriate modifications, other data assimilation techniques, and other models, can be readily substituted.

The approach taken here is global in the sense that the coefficients c_j^i are constant in phase space. To the extent that the data makes it practical, it may be beneficial to develop a further extension of these ideas that treats the data more locally.

Although we demonstrate its use for variables that do not appear in the model, the method can be beneficial in cases of poorly-modeled variables, or in general when model

error is significant. The success of the method will depend on the choice of the multiple models. We have found that the method works well when using neural models to reconstruct quantities that are not included among the model variables. Its use will be crucial for experiments on control of spreading depression and seizures in neural cultures, where extensive, realtime measurements of potassium and calcium concentrations are needed but are not feasible, while voltages are easily available. We expect the method to find application in a variety of physics, geophysics and biological contexts where current models are poor or nonexistent.

Appendix A: Appendix

A.1 Rederiving Kalman Filter Equations

An alternative formulation of the Kalman filter equations can be derived that allows for ease of implementation in nonlinear filtering schemes. The following derivation follows that found in [54] though more details are shown here. Assume a linear discrete-time system

$$\begin{aligned} x(k) &= F(k-1)x(k-1) + w(k-1) \\ y(k) &= A(k)x(k) + v(k) \end{aligned}$$

where $w(k)$ and $v(k)$ are independent and zero-mean with respective covariances $Q(k)$ and $R(k)$.

Let us assume that we have an a priori estimate $\hat{x}^-(k)$ at time k. We would like to update this state based on a measurement taken at time k. We update the state estimate with the following linear equation

$$\hat{x}^+(k) = K(k)y(k) + b(k)$$

From this point on we will drop the k in notation and equations for the sake of brevity. We know that for a general random vector z that

$$\begin{aligned} P_z &= E[(z-\bar{z})(z-\bar{z})^T] \\ &= E[zz^T] - \bar{z}\bar{z}^T \end{aligned}$$

We are interested in minimizing the trace of the following matrix

$$P_x^+ = E[(x-\hat{x}^+)(x-\hat{x}^+)^T]$$

Why the trace? Essentially we would like to minimize the 2-norm of the matrix (Frobenius norm) which is defined as

$$||A||_2 = \sqrt{trace(AA^*)}$$

where A is an arbitrary matrix.

If we define $z = x - \hat{x}^+$ we have

$$\begin{aligned} P_x^+ &= E[(x - \hat{x}^+)(x - \hat{x}^+)^T] \\ &= E[zz^T] \\ &= P_z + \bar{z}\bar{z}^T \end{aligned}$$

We calculate P_z as follows:

$$
\begin{aligned}
P_z &= E[((x-\hat{x}^+)-E(x-\hat{x}^+))(\ldots)^T] \\
&= E[((x-\hat{x}^+)-(\bar{x}-(K\bar{y}+b)))(\ldots)^T] \\
&= E[((x-(Ky+b))-(\bar{x}-(K\bar{y}+b)))(\ldots)^T] \\
&= E[(x-Ky-b-\bar{x}+K\bar{y}+b)(\ldots)^T] \\
&= E[(x-\bar{x}-K(y-\bar{y}))(\ldots)^T] \\
&= E[(x-\bar{x}-K(y-\bar{y}))(x-\bar{x}-K(y-\bar{y}))^T] \\
&= E[xx^T-x\bar{x}^T-x(K(y-\bar{y}))^T-\bar{x}x^T+\bar{x}\bar{x}^T+\bar{x}(K(y-\bar{y}))^T \\
&- K(y-\bar{y})x^T+K(y-\bar{y})\bar{x}^T+K(y-\bar{y})(K(y-\bar{y}))^T] \\
&= E[xx^T-x\bar{x}^T-\bar{x}x^T+\bar{x}\bar{x}^T]+E[-K(y-\bar{y})x^T+K(y-\bar{y})\bar{x}^T] \\
&+ E[-x(K(y-\bar{y}))^T+\bar{x}(K(y-\bar{y}))^T]+E[K(y-\bar{y})(K(y-\bar{y}))^T] \\
&= E[(x-\bar{x})(x-\bar{x})^T]-KE[(y-\bar{y})(x-\bar{x})^T]-E[(x-\bar{x})(y-\bar{y})^T]K^T+KE[(y-\bar{y})(y-\bar{y})^T]K^T \\
&= P_x^- - KP_{yx} - P_{xy}K^T + KP_yK^T
\end{aligned}
$$

Now we can calculate

$$
\begin{aligned}
P_x^+ &= P_z + \bar{z}\bar{z}^T \\
&= P_x^- - KP_{yx} - P_{xy}K^T + KP_yK^T + E[x-\hat{x}^+](E[x-\hat{x}^+])^T \\
&= P_x^- - KP_{yx} - P_{xy}K^T + KP_yK^T + (\bar{x}-K\bar{y}-b)(\bar{x}-K\bar{y}-b)^T \\
&= (K-P_{xy}P_y^{-1})P_y(K-P_{xy}P_y^{-1})^T + (P_x^- - P_{xy}P_y^{-1}P_{xy}^T) + (\bar{x}-K\bar{y}-b)(\bar{x}-K\bar{y}-b)^T
\end{aligned}
$$

Now,

$$\begin{aligned} Tr(P_x^+) &= Tr((K - P_{xy}P_y^{-1})P_y(K - P_{xy}P_y^{-1})^T + (P_x^- - P_{xy}P_y^{-1}P_{xy}^T) + (\bar{x} - K\bar{y} - b)(\bar{x} - K\bar{y} - b)^T) \\ &= Tr((K - P_{xy}P_y^{-1})P_y(K - P_{xy}P_y^{-1})^T) + Tr(P_x^- - P_{xy}P_y^{-1}P_{xy}^T) \\ &+ Tr((\bar{x} - K\bar{y} - b)(\bar{x} - K\bar{y} - b)^T) \end{aligned}$$

It is clear that to minimize the above we set

$$\begin{aligned} K &= P_{xy}P_y^{-1} \\ b &= \bar{x} - K\bar{y} \end{aligned}$$

This then allows us to write the following equations

$$\begin{aligned} \hat{x}^+ &= Ky + b \\ &= Ky + \bar{x} - K\bar{y} \\ &= Ky + \hat{x}^- - KA\hat{x}^- \\ &= \hat{x}^- + K(y - A\hat{x}^-) \\ P_x^+ &= P_x^- - P_{xy}P_y^{-1}P_{yx} \end{aligned}$$

We also see that

$$\begin{aligned}
P_{xy} &= E[(x-\bar{x})(y-\bar{y})^T] \\
&= E[(x-\bar{x})(Ax+v-A\bar{x})^T] \\
&= E[(x-\bar{x})(x^TA^T+v^T-\bar{x}^TA^T)] \\
&= E[xx^TA^T+xv^T-x\bar{x}^TA^T-\bar{x}x^TA^T-\bar{x}v^T+\bar{x}\bar{x}^TA^T] \\
&= E[xx^T-x\bar{x}^T-\bar{x}x^T+\bar{x}\bar{x}^T]A^T+E[xv^T-\bar{x}v^T] \\
&= P_x^-A^T
\end{aligned}$$

and

$$\begin{aligned}
P_y &= E[(y-\bar{y})(y-\bar{y})^T] \\
&= E[yy^T-y\bar{y}^T-\bar{y}y^T+\bar{y}\bar{y}^T] \\
&= E[(Ax+v)(x^TA^T+v^T)-(Ax+v)\bar{x}^TA^T-A\bar{x}(x^TA^T+v^T)+A\bar{x}\bar{x}^TA^T] \\
&= AE[xx^T-x\bar{x}^T-\bar{x}x^+\bar{x}\bar{x}^T]A^T+E[vv^T]+E[Axv^T+vx^TA^T+v\bar{x}^TA^T-A\bar{x}v^T] \\
&= AP_x^-A^T+R
\end{aligned}$$

The equations for K and P_x^- are different from the ones derived earlier:

$$K = P_x^-A^T(AP_x^-A^T+R)^{-1} \rightarrow P_{xy}P_y^{-1} \tag{A.1}$$

$$P_x^+ = (I-KA)P_x^- \rightarrow P_x^- - P_{xy}P_y^{-1}P_{yx} \tag{A.2}$$

We show this first for Equation A.1:

$$\begin{aligned}
K &= P_x^-A^T(AP_x^-A^T+R)^{-1} \\
&= P_{xy}P_y^{-1}
\end{aligned}$$

We now show this for Equation A.2:

$$\begin{aligned} P_x^+ &= (I - KA)P_x^- \\ &= P_x^- - KAP_x^- \\ &= P_x^- - P_{xy}P_y^{-1}AP_x^- \\ &= P_x^- - P_{xy}P_y^{-1}(P_x^-A^T)^T \\ &= P_x^- - P_{xy}P_y^{-1}(P_{xy})^T \\ &= P_x^- - P_{xy}P_y^{-1}P_{yx} \end{aligned}$$

In summary, we have the following equations for implementing the Kalman filter:

$$\begin{aligned} \hat{x}^-(k) &= F(k-1)\hat{x}^+(k-1) \\ P_x^-(k) &= F(k-1)P_x^+(k-1)F^T(k-1) + Q(k) \\ P_{xy} &= P_x^-A^T \\ P_y &= AP_x^-A^T + R \\ \hat{x}^+(k) &= \hat{x}^-(k) + K(k)(y(k) - A(k)\hat{x}^-(k)) \\ P_x^+(k) &= P_x^-(k) - P_{xy}P_y^{-1}P_{yx} \end{aligned}$$

A.2 Error in Approximating Nonlinear Systems

The following derivation follows that found in [54], but more details are included here. Let us consider a general nonlinear transformation

$$y = h(x)$$

where x is an $n \times 1$ vector. We write a Taylor series expansion of the above around the point $x = \bar{x}$ defining $\tilde{x} = x - \bar{x}$ as a zero-mean random variable with a symmetric probability

density function (pdf):

$$\begin{aligned} y &= h(x) \\ &= h(\bar{x}) + D_{\tilde{x}}h + \frac{1}{2!}D_{\tilde{x}}^2 h + \frac{1}{3!}D_{\tilde{x}}^3 h + \dots \end{aligned}$$

where

$$D_{\tilde{x}}^k h = \left(\sum_{i=1}^{n} \tilde{x}_i \frac{\partial}{\partial x_i} \right)^k h(x) \Big|_{x=\bar{x}}$$

Now we first would like to find the mean of y, $\bar{y}$:

$$\begin{aligned} \bar{y} &= E\left[h(\bar{x}) + D_{\tilde{x}}h + \frac{1}{2!}D_{\tilde{x}}^2 h + \frac{1}{3!}D_{\tilde{x}}^3 h + \dots \right] \\ &= h(\bar{x}) + E\left[D_{\tilde{x}}h + \frac{1}{2!}D_{\tilde{x}}^2 h + \frac{1}{3!}D_{\tilde{x}}^3 h + \dots \right] \end{aligned}$$

Before we work with this further, let us consider a random variable X that has zero mean and symmetric pdf (i.e. $f_X(x) = f_X(-x)$). In calculating the i^{th} moment of X (where i is

odd) we see

$$\begin{aligned}
E[X^i] &= \int_{-\infty}^{\infty} x^i f_X(x)dx \\
&= \int_{-\infty}^{0} x^i f_X(x)dx + \int_{0}^{\infty} x^i f_X(x)dx \\
&= -\int_{-\infty}^{0} (-x)^i f_X(-x)dx + \int_{0}^{\infty} x^i f_X(x)dx \\
&= \int_{0}^{\infty} (-x)^i f_X(x)dx + \int_{0}^{\infty} x^i f_X(x)dx \\
&= -\int_{0}^{\infty} x^i f_X(x)dx + \int_{0}^{\infty} x^i f_X(x)dx \\
&= 0
\end{aligned}$$

Now, when x is a vector this same argument holds although the formulation above is slightly different. Looking at $E[D_{\tilde{x}}h]$ we see

$$\begin{aligned}
E[D_{\tilde{x}}h] &= E\left[\sum_{i=1}^{n} \tilde{x}_i \frac{\partial}{\partial x_i} h(x)\Big|_{x=\bar{x}}\right] \\
&= \sum_{i=1}^{n} E[\tilde{x}_i] \frac{\partial}{\partial x_i} h(x)\Big|_{x=\bar{x}} \\
&= 0
\end{aligned}$$

and likewise all all odd order terms will also be equal to zero. As such

$$\bar{y} = h(\bar{x}) + \frac{1}{2!}E[D_{\tilde{x}}^2 h] + \frac{1}{4!}E[D_{\tilde{x}}^4 h] + \ldots \tag{A.3}$$

In addition to the mean $\bar{y}$ we would also like to find the covariance of y, P_y where

$$P_y = E[(y - \bar{y})(y - \bar{y})^T]$$

Now, $y - \bar{y}$ is

$$\begin{aligned} y - \bar{y} &= \left[h(\bar{x}) + D_{\tilde{x}}h + \frac{1}{2!}D_{\tilde{x}}^2 h + \frac{1}{3!}D_{\tilde{x}}^3 h + \ldots\right] - \left[h(\bar{x}) + \frac{1}{2!}E[D_{\tilde{x}}^2 h] + \frac{1}{4!}E[D_{\tilde{x}}^4 h] + \ldots\right] \\ &= \left[D_{\tilde{x}}h + \frac{1}{2!}D_{\tilde{x}}^2 + \ldots\right] + \left[\frac{1}{2!}E[D_{\tilde{x}}^2 h] + \frac{1}{4!}E[D_{\tilde{x}}^4 h] + \ldots\right] \end{aligned}$$

Going back to our definition of P_y

$$\begin{aligned} P_y &= E[(y - \bar{y})(y - \bar{y})^T] \\ &= E\left[\left(D_{\tilde{x}}h + \frac{1}{2!}D_{\tilde{x}}^2 h + \ldots + \frac{1}{2!}E[D_{\tilde{x}}^2 h] + \frac{1}{4!}E[D_{\tilde{x}}^4 h] + \ldots\right)(\ldots)^T\right] \\ &= E\left[D_{\tilde{x}}hD_{\tilde{x}}^T h + \frac{D_{\tilde{x}}h(D_{\tilde{x}}^2 h)^T}{2!} + \frac{D_{\tilde{x}}h(D_{\tilde{x}}^3 h)^T}{3!} + \ldots + E\left[\frac{D_{\tilde{x}}^2 h}{2!}\right]E\left[\frac{D_{\tilde{x}}^2 h}{2!}\right]^T + \ldots\right] \end{aligned}$$

Much like before, we note that the odd order terms fall out. As such

$$\begin{aligned} P_y &= E\left[D_{\tilde{x}}hD_{\tilde{x}}^T h + \frac{D_{\tilde{x}}h(D_{\tilde{x}}^2 h)^T}{2!} + \frac{D_{\tilde{x}}h(D_{\tilde{x}}^3 h)^T}{3!} + \ldots + E\left[\frac{D_{\tilde{x}}^2 h}{2!}\right]E\left[\frac{D_{\tilde{x}}^2 h}{2!}\right]^T + \ldots\right] \\ &= E\left[D_{\tilde{x}}hD_{\tilde{x}}^T h + \frac{D_{\tilde{x}}h(D_{\tilde{x}}^3 h)^T}{3!} + \ldots + E\left[\frac{D_{\tilde{x}}^2 h}{2!}\right]E\left[\frac{D_{\tilde{x}}^2 h}{2!}\right]^T + \ldots\right] \\ &= E[D_{\tilde{x}}hD_{\tilde{x}}^T h] + E\left[\frac{D_{\tilde{x}}h(D_{\tilde{x}}^3 h)^T}{3!} + \ldots\right] + E\left[\frac{D_{\tilde{x}}^2 h}{2!}\right]E\left[\frac{D_{\tilde{x}}^2 h}{2!}\right]^T + \ldots \end{aligned}$$

We can write the first term as

$$\begin{aligned}
E[D_{\tilde{x}} h D_{\tilde{x}}^T h] &= E\left[\left(\sum_{i=1}^{n} \tilde{x}_i \frac{\partial h}{\partial x_i}\Big|_{x=\bar{x}}\right)\left(\sum_{j=1}^{n} \tilde{x}_j \frac{\partial h}{\partial x_j}\Big|_{x=\bar{x}}\right)^T\right] \\
&= E\left[\sum_{i,j} \tilde{x}_i \frac{\partial h}{\partial x_i}\Big|_{x=\bar{x}} \frac{\partial h^T}{\partial x_j}\Big|_{x=\bar{x}} \tilde{x}_j\right] \\
&= \sum_{i,j} E\left[\tilde{x}_i \frac{\partial h}{\partial x_i}\Big|_{x=\bar{x}} \frac{\partial h^T}{\partial x_j}\Big|_{x=\bar{x}} \tilde{x}_j\right] \\
&= \sum_{i,j} \frac{\partial h}{\partial x_i}\Big|_{x=\bar{x}} E\left[\tilde{x}_i \tilde{x}_j\right] \frac{\partial h^T}{\partial x_j}\Big|_{x=\bar{x}} \\
&= \sum_{i,j} H_i P_{ij} H_j^T \\
&= HPH^T
\end{aligned}$$

We can now write the covariance of y as

$$P_y = HPH^T + E\left[\frac{D_{\tilde{x}} h (D_{\tilde{x}}^3 h)^T}{3!} + \ldots\right] + E\left[\frac{D_{\tilde{x}}^2 h}{2!}\right] E\left[\frac{D_{\tilde{x}}^2 h}{2!}\right]^T + \ldots \tag{A.4}$$

A.2.1 Approximation through Linearization

One way to approximate the nonlinear transformation h is to linearize the system

$$\begin{aligned}
y &= h(x) \\
&\approx h(\bar{x}) + \frac{\partial h}{\partial x}\Big|_{x=\bar{x}} \tilde{x}
\end{aligned}$$

We can calculate the mean of the linearized system $\bar{y}_\ell$,

$$\begin{aligned}
\bar{y} &= E\left[h(x)\right] \\
&\approx E\left[h(\bar{x}) + \left.\frac{\partial h}{\partial x}\right|_{x=\bar{x}} \tilde{x}\right] \\
&= h(\bar{x}) + \left.\frac{\partial h}{\partial x}\right|_{x=\bar{x}} E[\tilde{x}] \\
&= h(\bar{x})
\end{aligned}$$

which is accurate up to first order in comparison to equation A.3. Additionally we can calculate the covariance of the linearized system P_ℓ

$$\begin{aligned}
P_\ell &= E[(y-\bar{y})(y-\bar{y})^T] \\
&\approx E\left[\left(h(\bar{x}) + \left.\frac{\partial h}{\partial x}\right|_{x=\bar{x}} \tilde{x} - h(\bar{x})\right)(\ldots)^T\right] \\
&= E\left[\left(\left.\frac{\partial h}{\partial x}\right|_{x=\bar{x}} \tilde{x}\right)\left(\left.\frac{\partial h}{\partial x}\right|_{x=\bar{x}} \tilde{x}\right)^T\right] \\
&= \left.\frac{\partial h}{\partial x}\right|_{x=\bar{x}} E\left[\tilde{x}\tilde{x}^T\right] \left.\frac{\partial h^T}{\partial x}\right|_{x=\bar{x}} \\
&= HPH^T
\end{aligned}$$

which is accurate up to second order in comparison to equation A.4. The approximation of h by linearization causes us to lose a fair amount of accuracy in representing the true mean and covariance of the system.

A.2.2 Approximation through the Unscented Transformation

We once again assume a nonlinear transformation

$$y = h(x)$$

The idea behind the unscented transformation [54–56] is to select a set of sigma points whose ensemble mean and covariance are equal to the known mean $\bar{x}$ and covariance P of x. The nonlinear transformation h is applied to each sigma point, resulting in a set of transformed sigma points. The ensemble mean and covariance of these transformed sigma points gives us an approximation of the true mean and covariance of y.

The $2n$ sigma points $x^{(i)}$ are defined as follows

$$\begin{aligned} x^{(i)} &= \bar{x} + \tilde{x}^{(i)} \qquad i = 1, \ldots, 2n \\ \tilde{x}^{(i)} &= (\sqrt{nP})_i^T \qquad i = 1, \ldots, n \\ \tilde{x}^{(n+i)} &= -(\sqrt{nP})_i^T \quad i = 1, \ldots, n \end{aligned}$$

The nonlinear function is applied to each sigma point resulting in the following transformed sigma points

$$y^{(i)} = h\left(x^{(i)}\right) \qquad i = 1, \ldots, 2n$$

Like before, we are interested in finding the mean of y. We denote by $\bar{y}$ the true mean of y and $\bar{y}_u$ the approxmated mean of y resulting from the unscented transformation. We write

$$\bar{y}_u = \sum_{i=1}^{2n} W^{(i)} y^{(i)}$$

where

$$W^{(i)} = \frac{1}{2n} \qquad i = 1, \ldots, 2n$$

As such we can write

$$\bar{y}_u = \frac{1}{2n}\sum_{i=1}^{2n} y^{(i)}$$

We expand this in a Taylor series around $\bar{x}$ which gives

$$\begin{aligned}
\bar{y}_u &= \frac{1}{2n}\sum_{i=1}^{2n}\left(h(\bar{x}) + D_{\tilde{x}^{(i)}}h + \frac{1}{2!}D^2_{\tilde{x}^{(i)}}h + \ldots\right) \\
&= h(\bar{x}) + \frac{1}{2n}\sum_{i=1}^{2n}\left(D_{\tilde{x}^{(i)}}h + \frac{1}{2!}D^2_{\tilde{x}^{(i)}}h + \ldots\right)
\end{aligned}$$

Let us examine the odd terms in the above series. For any $k \geq 0$ we see

$$\begin{aligned}
\sum_{j=1}^{2n} D^{2k+1}_{\tilde{x}^{(j)}}h &= \sum_{j=1}^{2n}\left[\left(\sum_{i=1}^{n}\tilde{x}_i^{(j)}\frac{\partial}{\partial x_i}\right)^{2k+1} h(x)\Big|_{x=\bar{x}}\right] \\
&= \sum_{j=1}^{2n}\left[\sum_{i=1}^{n}\left(\tilde{x}_i^{(j)}\right)^{2k+1}\frac{\partial^{2k+1}}{\partial x_i^{2k+1}}h(x)\Big|_{x=\bar{x}}\right] \\
&= \sum_{i=1}^{n}\left[\sum_{j=1}^{2n}\left(\tilde{x}_i^{(j)}\right)^{2k+1}\frac{\partial^{2k+1}}{\partial x_i^{2k+1}}h(x)\Big|_{x=\bar{x}}\right] \\
&= 0
\end{aligned}$$

Based on the sigma points we defined earlier, $\tilde{x}^{(j)} = -\tilde{x}^{(n+j)}$ where $j = 1, \ldots, n$. For all odd terms, the odd power will preserve the negative sign in the $-\tilde{x}^{(n+j)}$ term. Thus all the terms in the sum will cancel out.

This leaves us with

$$\begin{aligned}\bar{y}_u &= h(\bar{x}) + \frac{1}{2n}\sum_{i=1}^{2n}\left(\frac{1}{2!}D^2_{\tilde{x}^{(i)}}h + \frac{1}{4!}D^4_{\tilde{x}^{(i)}}h + \ldots\right) \\ &= h(\bar{x}) + \frac{1}{2n}\sum_{i=1}^{2n}\frac{1}{2!}D^2_{\tilde{x}^{(i)}}h + \sum_{i=1}^{2n}\left(\frac{1}{4!}D^4_{\tilde{x}^{(i)}}h + \frac{1}{6!}D^6_{\tilde{x}^{(i)}}h + \ldots\right)\end{aligned}$$

By expanding the second term we see

$$\begin{aligned}\frac{1}{2n}\sum_{i=1}^{2n}\frac{1}{2!}D^2_{\tilde{x}^{(i)}}h &= \frac{1}{2n}\sum_{k=1}^{2n}\frac{1}{2!}\left(\sum_{i=1}^{n}\tilde{x}_i^{(k)}\frac{\partial}{\partial x_i}\right)^2 h(x)\Big|_{x=\bar{x}} \\ &= \frac{1}{4n}\sum_{k=1}^{2n}\sum_{i,j=1}^{n}\tilde{x}_i^{(k)}\tilde{x}_j^{(k)}\frac{\partial^2}{\partial x_i \partial x_j}h(x)\Big|_{x=\bar{x}} \\ &= \frac{1}{4n}\sum_{i,j=1}^{n}\sum_{k=1}^{2n}\tilde{x}_i^{(k)}\tilde{x}_j^{(k)}\frac{\partial^2}{\partial x_i \partial x_j}h(x)\Big|_{x=\bar{x}}\end{aligned}$$

and since $\tilde{x}^{(k)} = -\tilde{x}^{(k+n)}$,

$$\sum_{k=1}^{2n}\tilde{x}_i^{(k)}\tilde{x}_j^{(k)} = 2\sum_{k=1}^{n}\tilde{x}_i^{(k)}\tilde{x}_j^{(k)}$$

which allows us to write

$$\begin{aligned}
\frac{1}{2n}\sum_{i=1}^{2n}\frac{1}{2!}D^2_{\tilde{x}^{(i)}}h &= \frac{1}{4n}\sum_{i,j=1}^{n}\sum_{k=1}^{2n}\tilde{x}_i^{(k)}\tilde{x}_j^{(k)}\frac{\partial^2}{\partial x_i\partial x_j}h(x)\Big|_{x=\bar{x}} \\
&= \frac{1}{2n}\sum_{i,j=1}^{n}\sum_{k=1}^{n}\tilde{x}_i^{(k)}\tilde{x}_j^{(k)}\frac{\partial^2}{\partial x_i\partial x_j}h(x)\Big|_{x=\bar{x}} \\
&= \frac{1}{2n}\sum_{i,j=1}^{n}\sum_{k=1}^{n}\left(\sqrt{nP}\right)_{ki}\left(\sqrt{nP}\right)_{kj}\frac{\partial^2}{\partial x_i\partial x_j}h(x)\Big|_{x=\bar{x}} \\
&= \frac{1}{2n}\sum_{i,j=1}^{n}nP_{ij}\frac{\partial^2}{\partial x_i\partial x_j}h(x)\Big|_{x=\bar{x}} \\
&= \frac{1}{2}\sum_{i,j=1}^{n}P_{ij}\frac{\partial^2}{\partial x_i\partial x_j}h(x)\Big|_{x=\bar{x}}
\end{aligned}$$

Therefore the approximate mean calculated through the unscented transformation is

$$\bar{y}_u = h(\bar{x}) + \frac{1}{2}\sum_{i,j=1}^{n}P_{ij}\frac{\partial^2}{\partial x_i\partial x_j}h(x)\Big|_{x=\bar{x}} + \frac{1}{2n}\sum_{i=1}^{2n}\left(\frac{1}{4!}D^4_{\tilde{x}^{(i)}}h + \frac{1}{6!}D^6_{\tilde{x}^{(i)}}h + \ldots\right)$$

We compare this with equation A.3, where the term $\frac{1}{2!}E[D_{\tilde{x}}^2 h]$ can be written as

$$\begin{aligned}
\frac{1}{2!}E[D_{\tilde{x}}^2 h] &= \frac{1}{2!}E\left[\left(\sum_{i=1}^{n}\tilde{x}_i\frac{\partial}{\partial x_i}\right)^2 h(x)\Big|_{x=\bar{x}}\right] \\
&= \frac{1}{2!}E\left[\sum_{i,j=1}^{n}\tilde{x}_i\tilde{x}_j\frac{\partial^2}{\partial x_i\partial x_j}h(x)\Big|_{x=\bar{x}}\right] \\
&= \frac{1}{2!}\sum_{i,j=1}^{n}E\left[\tilde{x}_i\tilde{x}_j\right]\frac{\partial^2}{\partial x_i\partial x_j}h(x)\Big|_{x=\bar{x}} \\
&= \frac{1}{2}\sum_{i,j=1}^{n}P_{ij}\frac{\partial^2}{\partial x_i\partial x_j}h(x)\Big|_{x=\bar{x}}
\end{aligned}$$

which allows us to write equation A.3 as

$$\bar{y} = h(\bar{x}) + \frac{1}{2}\sum_{i,j=1}^{n}P_{ij}\frac{\partial^2}{\partial x_i\partial x_j}h(x)\Big|_{x=\bar{x}} + \frac{1}{4!}E[D_{\tilde{x}}^4 h] + \frac{1}{6!}E[D_{\tilde{x}}^6 h] + \ldots$$

Therefore, $\bar{y}_u$ is accurate up to third order. This already represents a signifcant improvement over linearization whose estimate of the mean was only accurate up to first order terms.

We now look to calculate the covariance approximation P_u resulting from the unscented

transformation. We define

$$\begin{aligned}
P_u &= E\left[\sum_{i=1}^{2n} W^{(i)}\left(y^{(i)}-\bar{y}_u\right)\left(y^{(i)}-\bar{y}_u\right)^T\right] \\
&= \frac{1}{2n}E\left[\sum_{i=1}^{2n}\left(y^{(i)}-\bar{y}_u\right)\left(y^{(i)}-\bar{y}_u\right)^T\right] \\
&= \frac{1}{2n}E\left[\sum_{i=1}^{2n}\left(h\left(x^{(i)}\right)-\bar{y}_u\right)\left(h\left(x^{(i)}\right)-\bar{y}_u\right)^T\right] \\
&= \frac{1}{2n}E\left[\sum_{i=1}^{2n}\left(h(\bar{x})+D_{\tilde{x}^{(i)}}h+\frac{1}{2!}D^2_{\tilde{x}^{(i)}}h+\ldots-h(\bar{x})-\frac{1}{2n}\sum_{i=1}^{2n}\frac{1}{2!}D^2_{\tilde{x}^{(i)}}h+\frac{1}{4!}D^4_{\tilde{x}^{(i)}}h+\ldots\right)(\ldots)^T\right]
\end{aligned}$$

Noting that $\tilde{x}^{(i)} = -\tilde{x}^{(i+n)}$ for $i = 1, \ldots, n$, the odd power terms above will equal 0 using the same reasoning from before. The majority of the terms will be higher order, and we

will neglect them. From here we have

$$
\begin{aligned}
P_u &= \frac{1}{2n}E\left[\sum_{i=1}^{2n}\left(D_{\tilde{x}^{(i)}}h+\frac{1}{2!}D^2_{\tilde{x}^{(i)}}h+\ldots-\frac{1}{2n}\sum_{i=1}^{2n}\frac{1}{2!}D^2_{\tilde{x}^{(i)}}h+\frac{1}{4!}D^4_{\tilde{x}^{(i)}}h+\ldots\right)(\ldots)^T\right]\\
&= \frac{1}{2n}E\left[\sum_{i=1}^{2n}\left(D_{\tilde{x}^{(i)}}h\right)\left(D_{\tilde{x}^{(i)}}h+\frac{1}{2!}D^2_{\tilde{x}^{(i)}}h+\ldots-\frac{1}{2n}\sum_{i=1}^{2n}\frac{1}{2!}D^2_{\tilde{x}^{(i)}}h+\frac{1}{4!}D^4_{\tilde{x}^{(i)}}h+\ldots\right)^T+H.O.T\right]\\
&= \frac{1}{2n}\sum_{i=1}^{2n}E\left[\left(D_{\tilde{x}^{(i)}}h\right)\left(D_{\tilde{x}^{(i)}}h\right)^T\right]+H.O.T\\
&= \frac{1}{2n}E\left[\sum_{i=1}^{2n}\sum_{j,k=1}^{n}\left(\tilde{x}^{(i)}_j\frac{\partial}{\partial x_j}h(x)\Big|_{x=\bar{x}}\right)\left(\tilde{x}^{(i)}_k\frac{\partial}{\partial x_k}h(x)\Big|_{x=\bar{x}}\right)^T\right]+H.O.T\\
&= \frac{1}{2n}E\left[\sum_{j,k=1}^{n}\sum_{i=1}^{2n}\left(\tilde{x}^{(i)}_j\frac{\partial}{\partial x_j}h(x)\Big|_{x=\bar{x}}\right)\left(\tilde{x}^{(i)}_k\frac{\partial}{\partial x_k}h(x)\Big|_{x=\bar{x}}\right)^T\right]+H.O.T\\
&= \frac{1}{n}E\left[\sum_{j,k=1}^{n}\sum_{i=1}^{n}\left(\tilde{x}^{(i)}_j\frac{\partial}{\partial x_j}h(x)\Big|_{x=\bar{x}}\right)\left(\tilde{x}^{(i)}_k\frac{\partial}{\partial x_k}h(x)\Big|_{x=\bar{x}}\right)^T\right]+H.O.T\\
&= \frac{1}{n}E\left[\sum_{j,k=1}^{n}\left(\frac{\partial}{\partial x_j}h(x)\Big|_{x=\bar{x}}\right)\left(\sum_{i=1}^{n}\left(\tilde{x}^{(i)}_j\right)\left(\tilde{x}^{(i)}_k\right)^T\right)\left(\frac{\partial}{\partial x_k}h(x)\Big|_{x=\bar{x}}\right)^T\right]+H.O.T\\
&= \frac{1}{n}\sum_{j,k=1}^{n}\left(\frac{\partial}{\partial x_j}h(x)\Big|_{x=\bar{x}}\right)\left(\sum_{i=1}^{n}E\left[\left(\tilde{x}^{(i)}_j\right)\left(\tilde{x}^{(i)}_k\right)^T\right]\right)\left(\frac{\partial}{\partial x_k}h(x)\Big|_{x=\bar{x}}\right)^T+H.O.T\\
&= \sum_{j,k=1}^{n}\left(\frac{\partial}{\partial x_j}h(x)\Big|_{x=\bar{x}}\right)P_{jk}\left(\frac{\partial}{\partial x_k}h(x)\Big|_{x=\bar{x}}\right)^T+H.O.T\\
&= HPH^T+H.O.T
\end{aligned}
$$

which is accurate to second order in comparison with equation A.4. This is the same order of accuracy as linearization, but of note is that the unscented approximation includes the higher order terms of appropriate sign while linearization only includes HPH^T.

A.3 Model of ionically mediated bursting

The seizure model developed in [16] consists of five differential equations,

$$
\begin{aligned}
C\frac{dV}{dt} &= -I_{\mathrm{Na}} - I_{\mathrm{K}} - I_{\mathrm{Cl}} + I_{\mathrm{stim}} \\
\tau\frac{d[K]_o}{dt} &= \gamma\beta(I_K - 2I_{\mathrm{pump}}) - \tilde{I}_{\mathrm{glia}} - \tilde{I}_{\mathrm{diffusion}} \\
\tau\frac{d[Na]_i}{dt} &= -\gamma(I_{Na} + 3I_{\mathrm{pump}}) \\
\frac{dh}{dt} &= \phi\left[\alpha_h(V)(1-h) - \beta_h(V)h\right] \\
\frac{dn}{dt} &= \phi\left[\alpha_n(V)(1-n) - \beta_n(V)n\right]
\end{aligned}
$$

The first equation describes the spiking behavior where C is the membrane capacitance, V is the membrane potential, and the membrane ion current densities are defined as

$$
\begin{aligned}
I_{\mathrm{Na}} &= g_{\mathrm{Na}} m_\infty^3 h\,(V - E_{\mathrm{Na}}) + g_{\mathrm{NaL}}\,(V - E_{\mathrm{Na}}) \\
I_{\mathrm{K}} &= g_{\mathrm{K}} n^4\,(V - E_{\mathrm{K}}) + g_{\mathrm{KL}}\,(V - E_{\mathrm{K}}) \\
I_{\mathrm{Cl}} &= g_{\mathrm{ClL}}\,(V - E_{\mathrm{Cl}})
\end{aligned}
$$

I_{stim} is a stimulating Poisson spike train with parameter λ. The second and third differential equations model the time evolution of the local extracellular potassium and the intracellular sodium concentrations. In these equations the $\tilde{I}$s are molar currents (millimolars per second)

and depend on the ion concentrations as follows:

$$
\begin{aligned}
I_{\mathrm{p}} &= \frac{\rho}{\gamma}\left(\frac{1}{1+\exp\left(\frac{25.0-[Na]_i}{3.0}\right)}\right)\left(\frac{1}{1+\exp\left(5.5-[K]_o\right)}\right) \\
\tilde{I}_{\mathrm{diff}} &= \varepsilon\left([K]_o-[K^+]_{\mathrm{bath}}\right) \\
\tilde{I}_{\mathrm{glia}} &= \frac{G_{\mathrm{glia}}}{1.0+\exp\left(\frac{18.0-[K]_o}{2.5}\right)}.
\end{aligned}
$$

The fourth and fifth differential equations represent the gating variables where

$$
\begin{aligned}
\alpha_h(V) &= 0.07\exp\left(-\frac{V+44}{20}\right) \\
\beta_h(V) &= \frac{1}{1+\exp(-0.1(V+14))} \\
\alpha_n(V) &= \frac{0.01(V+34)}{1-\exp(-0.1(V+34))} \\
\beta_n(V) &= 0.125\exp\left(-\frac{V+44}{80}\right)
\end{aligned}
$$

For simplification, we follow [16] in making the assumption

$$
\begin{aligned}
[K]_i &= 140.0\ \mathrm{mM} + (18.0\ \mathrm{mM} - [Na]_i) \\
[Na]_o &= 144.0\ \mathrm{mM} - \beta\left([Na]_i - 18.0\ \mathrm{mM}\right).
\end{aligned}
$$

which allows us to define the sodium and potassium equilibrium potentials E_{Na} and E_K, respectively

$$E_K = 26.64 \ln \left(\frac{[K]_o}{[K]_i} \right)$$

$$E_{Na} = 26.64 \ln \left(\frac{[Na]_o}{[Na]_i} \right).$$

Bibliography

Bibliography

[1] G. Gross and J. Kowalski, "Origins of activity patterns in self-organizing neuronal networks in vitro," *Journal of Intelligent Material Systems and Structures*, vol. 10, pp. 558–564, 1999.

[2] G. Gross, G. Kreutzberg, and A. Meyer, "A new fixed-array multimicroelectrode system designed for long-term monitoring of extracellular single unit neuronal activity in vitro," *Neuroscience Letters*, vol. 6, pp. 101–105, 1977.

[3] G. Gross, "Simultaneous single unit recording in vitro with a photoetched laser deinsulated gold multi-microelectrode surface," *IEEE Transactions on Biomedical Engineering*, vol. 26, pp. 273–279, 1979.

[4] H. Charkhkar, C. Frewin, M. Nezafati, G. Knaack, N. Peixoto, S. Saddow, and J. Pancrazio, "Use of cortical neuronal networks for in vitro material biocompatibility testing," *Biosensors and Bioelectronics*, vol. 53, pp. 316–323, 2014.

[5] E. Keefer, A. Gramowski, and G. Gross, "Nmda receptor dependent periodic oscillations in cultured spinal cord networks," *Journal of Neurophysiology*, vol. 86, pp. 3030–3042, 2001.

[6] G. Knaack, H. Charkhkar, F. Hamilton, N. Peixoto, T. O'Shaughnessy, and J. Pancrazio, "Differential responses to ω-agatoxin iva in murine frontal cortex and spinal cord derived neuronal networks," *NeuroToxicology*, vol. 37, pp. 19–25, 2013.

[7] D. Wagenaar, R. Madhavan, and S. Potter, "Controlling bursting in cortical cultures with closed-loop multi-electrode stimulation," *Journal of Neuroscience*, vol. 25, pp. 680–688, 2005.

[8] D. Wagenaar, J. Pine, and S. Potter, "Effective parameters for stimulation of dissociated cultures using multi-electrode arrays," *Journal of Neuroscience Methods*, vol. 138, pp. 27–37, 2004.

[9] M. Chiappalone, P. Massobrio, and S. Martinoia, "Network plasticity in cortical assemblies," *Europen Journal of Neuroscience*, vol. 28, pp. 221–237, 2008.

[10] A. Pimashkin, A. Gladkov, I. Mukhina, and V. Kazantsev, "Adaptive enhancement of learning protocol in hippocampal cultured networks grown on multielectrode arrays," *Frontiers in Neural Circuits*, vol. 7, pp. 1–9, 2013.

[11] L. Bologna, T. Nieus, M. Tedesco, M. Chiappalone, F. Benfenati, and S. Martinoia, "Low-frequency stimulation enhances burst activity in cortical cultures during development," *Neuroscience*, vol. 165, pp. 692–704, 2010.

[12] F. Frohlich and D. McCormick, "Endogenous electric fields may guide neocortical network activity," *Neuron*, vol. 67, pp. 129–143, 2010.

[13] C. Anastassiou, R. Perin, H. Markram, and C. Koch, "Ephaptic coupling of cortical neurons," *Nature Neuroscience*, vol. 14, pp. 217–223, 2011.

[14] S. Ozen, A. Sirota, M. Belluscio, C. Anastassiou, E. Stark, C. Koch, and G. Buzaki, "Transcranial electric stimulation entrains cortical neuronal populations in rats," *Journal of Neuroscience*, vol. 30, pp. 11 476–11 485, 2010.

[15] A. Hodgkin and A. Huxley, "A quantitative description of membrane current and its application to conduction and excitation in nerve," *J. Physiology*, vol. 117, pp. 500–544, 1952.

[16] J. Cressman, G. Ullah, J. Ziburkus, S. Schiff, and E. Barreto, "The influence of sodium and potassium dynamics on excitability, seizures, and the stability of persistent states: I. single neuron dynamics," *Journal of Computational Neuroscience*, vol. 26, pp. 159–170, 2009.

[17] R. FitzHugh, "Impulses and physiological states in theoretical models of nerve membrane," *Biophysical Journal*, vol. 1, pp. 445–466, 1961.

[18] J. Nagumo, S. Arimoto, and S. Yoshizawa, "An active pulse transmission line simulating nerve axon," *Proceedings of the IEEE*, vol. 50, pp. 2061–2070, 1962.

[19] H. Wilson and J. Cowan, "Excitatory and inhibitory interactions in localized populations of model neurons," *Biophysical Journal*, vol. 12, pp. 1–24, 1972.

[20] J. Hindmarsh and R. Rose, "A model of neuronal bursting using three coupled first order differential equations," *Proc. Roy. Soc.*, vol. 221, pp. 87–102, 1984.

[21] E. M. Izhikevich, "Simple model of spiking neurons," *IEEE Transactions on Neural Networks*, vol. 14, no. 6, pp. 1569– 1572, Nov. 2003.

[22] E. Kalnay, *Atmospheric modeling, data assimilation, and predictability.* Cambridge Univ. Press, 2003.

[23] G. Evensen, *Data assimilation: The Ensemble Kalman Filter.* Springer: Heidelberg, 2009.

[24] F. Rabier, "Overview of global data assimilation developments in numerical weather-prediction centres," *Quarterly Journal of the Royal Meteorological Society*, vol. 131, no. 613, pp. 3215–3233, 2005.

[25] B. Hunt, E. Kalnay, and E. Kostelich, "Four-dimensional ensemble Kalman filtering," *Tellus A*, vol. 56, pp. 273–277, 2004.

[26] J. A. Cummings, "Operational multivariate ocean data assimilation," *Quarterly Journal of the Royal Meteorological Society*, vol. 131, no. 613, pp. 3583–3604, 2005.

[27] K. Yoshida, J. Yamaguchi, and Y. Kaneda, "Regeneration of small eddies by data assimilation in turbulence," *Phys. Rev. Lett.*, vol. 94, p. 014501, Jan 2005.

[28] K. Law and A. Stuart, "Evaluating data stimulation algorithms," *Mon. Wea. Rev.*, vol. 140, pp. 3757–3782, 2012.

[29] S. Schiff, *Neural control engineering.* MIT Press, 2012.

[30] T. Berry and T. Sauer, "Adaptive ensemble kalman filtering of nonlinear systems," *Tellus A*, vol. 65, p. 20331, 2013.

[31] G. Ullah and S. Schiff, "Assimilating seizure dynamics," *PLoS Computational Biology*, vol. 6, p. e1000776, 2010.

[32] M. Ruaro, P. Bonifazi, and V. Torre, "Toward the neurocomputer: image processing and pattern recognition with neuronal cultures," *IEEE Transactions on Biomedical Engineering*, vol. 52, pp. 371–383.

[33] M. Chiappalone, M. Bove, A. Vato, M. Tedesco, and S. Martinoia, "Dissociated cortical networks show spontaneously correlated activity patterns during in vitro development," *Brain Research*, vol. 1093, pp. 41–53, 2006.

[34] F. Hamilton, A. Akhavian, G. Knaack, H. Charkhkar, S. Minnikanti, W. Kim, J. Kastee, and N. Peixoto, "Dynamic steering of in vitro cortical neurons using field stimulation," *Proceedings of EMBC 36th Annual International Conference of the IEEE*, pp. 6577–6580, 2014.

[35] M. Bikson, J. Lian, P. Hahn, W. Stacey, C. Sciortino, and D. Durand, "Suppression of epileptiform activity by high frequency sinusoidal fields in rat hippocampal slices," *Journal of Physiology*, vol. 531, pp. 181–191, 2001.

[36] J. Selinger, N. Kulagina, T. O'Shaughnessy, W. Ma, and J. Pancrazio, "Methods for characterizing interspike intervals and identifying bursts in neuronal activity," *Journal of Neuroscience Methods*, vol. 162, p. 6471, 2007.

[37] W. Arnold and G. Fuhr, "Increasing the permittivity and conductivity of cellular electromanipulation media," *Industry Applications Society Annual Meeting Conference Record of the 1994 IEEE*, vol. 2, pp. 2–6, 1994.

[38] R. Kuczenski, H. Chang, and A. Revzin, "Dielectrophoretic microfluidic device for the continuous sorting of escherichia coli from blood cells," *Biomicrofluidics*, vol. 5, p. 032005, 2011.

[39] J. Kraus and D. Fleisch, *Electromagnetics with applications.* WCB McGraw-Hill, 1999.

[40] G. Shahaf and S. Marom, "Learning in networks of cortical neurons," *Journal of Neuroscience*, vol. 21, pp. 8782–8788, 2001.

[41] S. Marom and G. Shahaf, "Development, learning and memory in large random networks of cortical neurons: lessons beyond anatomy," *Q. Rev. Biophys.*, vol. 35, p. 6387, 2002.

[42] S. Marom and D. Eytan, "Learning in ex-vivo developing networks of cortical neurons," *Prog. Brain Res.*, vol. 147, pp. 189–199, 2005.

[43] Y. Li, W. Zhou, X. Li, S. Zeng, M. Liu, and Q. Luo, "Characterization of synchronized bursts in cultured hippocampal neuronal networks with learning training on microelectrode arrays," *Biosensors and Bioelectronics*, vol. 22, pp. 2976–2982, 2007.

[44] Y. Li, W. Zhou, X. Li, S. Zeng, and Q. Luo, "Dynamics of learning in cultured neuronal networks with antagonists of glutamate receptors," *Biophysical Journal*, vol. 93, pp. 4151–4158, 2007.

[45] J. le Feber, J. Stegenga, and W. Rutten, "The effect of slow electrical stimuli to achieve learning in cultured networks of rat cortical neurons," *PLoS ONE*, vol. 5, p. e8871.

[46] M. Dranias, H. Ju, E. Rajaram, and A. VanDougen, "Short-term memory in networks of dissociated cortical neurons," *The Journal of Neuroscience*, vol. 33, pp. 1940–1953, 2013.

[47] D. Eytan and S. Marom, "Dynamics and effective topology underlying synchronization in networks of cortical neurons," *The Journal of Neuroscience*, vol. 26, pp. 8465–8476, 2013.

[48] A. Gal, D. Eytan, A. Wallach, M. Sandler, J. Schiller, and S. Marom, "Dynamics of excitability over extended timescales in cultured cortical neurons," *The Journal of Neuroscience*, vol. 30, pp. 16 332–16 342, 2010.

[49] E. Kermany, A. Gal, V. Lyakhov, R. Meir, S. Marom, and D. Eytan, "Tradeoffs and constraints on neural representation in networks of cortical neurons," *The Journal of Neuroscience*, vol. 30, pp. 9588–9596, 2010.

[50] H. Voss, J. Timmer, and J. Kurths, "Nonlinear dynamical system identification from uncertain and indirect measurements," *Int. J. Bif. Chaos*, vol. 14, pp. 1905–1924, 2002.

[51] E. Baake, M. Baake, H. Bock, and K. Briggs, "Fitting ordinary differential equations to chaotic data," *Physical Review A*, vol. 45, 1992.

[52] H. Bock, "Recent advances in parameter identification for ordinary differential equations," *Progress in Scientific Computing*, vol. 2, pp. 95–121, 1983.

[53] R. Kalman, "A new approach to linear filtering and prediction problems," *J. Basic Eng.*, vol. 82, pp. 35–45, 1960.

[54] D. Simon, *Optimal State Estimation: Kalman, H_∞, and Nonlinear Approaches.* John Wiley and Sons, 2006.

[55] S. Julier, J. Uhlmann, and H. Durrant-Whyte, "A new method for the nonlinear transformation of means and covariances in filters and estimators," *IEEE Trans. Automat. Control*, vol. 45, pp. 477–482, 2000.

[56] ——, "Unscented filtering and nonlinear estimation," *Proc. IEEE*, vol. 92, pp. 401–422, 2004.

[57] R. Kopp and R. Orford, "Linear regression applied to system identification for adaptive control systems," *AIAA Journal*, vol. 1, pp. 2300–2306, 1963.

[58] H. Cox, "On the estimation of state variables and parameters for noisy dynamic systems," *IEEE Trans. Automatic Control*, vol. 9, pp. 5–12, 1964.

[59] E. Wan and A. Nelson, "Dual extended Kalman Filter methods," *Kalman Filtering and Neural Networks, Ed. S. Haykin*, pp. 123–173, 2001.

[60] C. Trudinger, M. Raupach, P. Rayner, and I. Enting, "Using the kalman filter for parameter estimation in biogeochemical models," *Environmetrics*, vol. 19, pp. 849–870, 2008.

[61] G. Ullah and S. Schiff, "Tracking and control of neuronal hodgkin-huxley dynamics," *Phys. Rev. E*, vol. 79, p. 040901, 2009.

[62] F. Hamilton, T. Berry, N. Peixoto, and T. Sauer, "Real-time tracking of neuronal network structure using data assimilation," *Physical Review E*, vol. 88, p. 052715, 2013.

[63] E. Lorenz, "Deterministic nonperiodic flow," *Journal of Atmospheric Sciences*, vol. 20, 1962.

[64] R. Dahlhaus, M. Eichler, and J. Sandkhler, "Identification of synaptic connections in neural ensembles by graphical models," *Journal of Neuroscience Methods*, vol. 77, no. 1, pp. 93–107, Nov. 1997.

[65] M. G. Rosenblum and A. S. Pikovsky, "Detecting direction of coupling in interacting oscillators," *Physical Review E*, vol. 64, p. 045202, 2001.

[66] D. Napoletani and T. D. Sauer, "Reconstructing the topology of sparsely connected dynamical networks," *Physical Review E*, vol. 77, no. 2, p. 026103, Feb. 2008.

[67] C. W. J. Granger, "Investigating causal relations by econometric models and cross-spectral methods," *Econometrica*, vol. 37, no. 3, pp. 424–438, 1969.

[68] L. Sommerlade, M. Thiel, B. Platt, A. Plano, G. Riedel, C. Grebogi, J. Timmer, and B. Schelter, "Inference of granger causal time-dependent influences in noisy multivariate time series," *Journal of Neuroscience Methods*, vol. 203, no. 1, pp. 173–185, Jan. 2012.

[69] D. R. Brillinger, "The identification of point process systems," *The Annals of Probability*, vol. 3, no. 6, pp. 909–924, Dec. 1975.

[70] A. Aertsen and G. Gerstein, "Evaluation of neuronal connectivity: Sensitivity of cross-correlation," *Brain Research*, vol. 340, pp. 341–54, 1984.

[71] A. M. Aertsen, G. L. Gerstein, M. K. Habib, and G. Palm, "Dynamics of neuronal firing correlation: modulation of "effective connectivity"," *Journal of Neurophysiology*, vol. 61, no. 5, pp. 900 –917, May 1989.

[72] M. Garofalo, T. Nieus, P. Massobrio, and S. Martinoia, "Evaluation of the performance of information Theory-Based methods and Cross-Correlation to estimate the functional connectivity in cortical networks," *PLoS ONE*, vol. 4, no. 8, p. e6482, 2009.

[73] E. S. Chornoboy, L. P. Schramm, and A. F. Karr, "Maximum likelihood identification of neural point process systems," *Biological Cybernetics*, vol. 59, no. 4-5, pp. 265–275, Sep. 1988.

[74] M. Okatan, M. A. Wilson, and E. N. Brown, "Analyzing functional connectivity using a network likelihood model of ensemble neural spiking activity," *Neural Computation*, vol. 17, no. 9, pp. 1927–1961, 2005.

[75] I. Stevenson, J. Rebesco, L. Miller, and K. Krding, "Inferring functional connections between neurons," *Current Opinion in Neurobiology*, vol. 17, 2008.

[76] I. H. Stevenson, J. M. Rebesco, N. G. Hatsopoulos, Z. Haga, L. E. Miller, and K. P. Kording, "Bayesian inference of functional connectivity and network structure from spikes," *IEEE Transactions on Neural Systems and Rehabilitation Engineering*, vol. 17, no. 3, pp. 203–213, Jun. 2009.

[77] G. N. Borisyuk, R. M. Borisyuk, A. B. Kirillov, E. I. Kovalenko, and V. I. Kryukov, "A new statistical method for identifying interconnections between neuronal network elements," *Biological Cybernetics*, vol. 52, no. 5, pp. 301–306, Sep. 1985.

[78] M. S. Masud and R. Borisyuk, "Statistical technique for analysing functional connectivity of multiple spike trains," *Journal of Neuroscience Methods*, vol. 196, no. 1, pp. 201–219, Mar. 2011.

[79] T. Berry, F. Hamilton, N. Peixoto, and T. Sauer, "Detecting connectivity changes in neuronal networks," *J. Neurosci. Meth.*, vol. 209, pp. 388–397, 2012.

[80] I. Belykh, E. d. Lange, and M. Hasler, "Synchronization of bursting neurons: what matters in the network topology," *Physical Review Letters*, vol. 94, p. 188101, 2005.

[81] D. Johnston and S. Miao-Sin Wu, *Foundations of cellular neurophysiology*. Bradford Books, 1995.

[82] H. Hasegawa, "Responses of a hodgkin-huxley neuron to various types of spike-train inputs," *Physical Review E*, vol. 61, pp. 718–726, 2000.

[83] S. Sipila, K. Huttu, I. Soltesz, J. Voipio, and K. Kaila, "Depolarizing gaba acts on intrinsically bursting pyramidal neurons to drive giant deploarizing potentials in the immature hippocampus," *The Journal of Neuroscience*, vol. 25, pp. 5280–5289, 2005.

[84] W. Ramadan, O. Eschenko, and S. Sara, "Hippocampal sharp wave/ripples during sleep for consolidation of associative memory," *PLoS One*, vol. 4, p. e6697, 2009.

[85] G. Buzsaki, "Large-scale recording of neuronal ensembles," *Nature Neuroscience*, vol. 7, pp. 446–451, 2004.

[86] M. Nicolelis, D. Dimitrov, J. Carmena, R. Crist, G. Lehew, J. Kralik, and S. Wise, "Chronic, multisite, multielectrode recordings in macaque monkeys," *Proceedings of the National Academy of Science*, vol. 100, pp. 11 041–11 046, 2003.

[87] F. Hamilton, J. Cressman, N. Peixoto, and T. Sauer, "Reconstructing neural dynamics using data assimilation with multiple models," *Europhysics Letters*, vol. 107, p. 68005, 2014.

[88] F. Takens, "Detecting strange attractors in turbulence," *Lecture Notes in Math. Springer-Verlag: Berlin*, vol. 898, 1981.

[89] N. Packard, J. Crutchfield, D. Farmer, and R. Shaw, "Geometry from a time series," *Phys. Rev. Lett.*, vol. 45, pp. 712–715, 1980.

[90] T. Sauer, J. Yorke, and M. Casdagli, "Embedology," *J. Stat. Phys.*, vol. 65, pp. 579–616, 1991.

[91] T. Sauer, "Reconstruction of shared nonlinear dynamics in a network," *Phys. Rev. Lett.*, vol. 93, pp. 198 701–4, 2004.

[92] E. Lorenz, "Deterministic nonperiodic flow," *J. Atmos. Sci.*, vol. 20, pp. 130–141, 1963.

[93] T. Krishnamurti, C. Kishtawal, and Z. Zhang, "Multimodel ensemble forecasts for weather and seasonal climate," *Science*, vol. 285, pp. 1548–1550, 1999.

[94] ——, "Multimodel ensemble forecasts for weather and seasonal climate," *Journal of Climate*, vol. 13, pp. 4196–4216, 2000.

[95] M. Athans and C. Chang, "Adaptive estimation and parameter identification using multiple model estimation algorithm," *U.S. Dept. of Commerce Tech. Report*, vol. AESD-TR-76-184, 1976.

[96] T. Palmer and J. Shukla, "A multimodel ensemble-based kalman filter for the retrieval of soil moisture profiles," *Q. J. Roy. Meterol. Soc.*, vol. 126, pp. 1989–1990, 2000.

[97] R. Hagedorn, F. Doblas-Reyes, and T. Palmer, "The rationale behind the success of multi-model ensembles in seasonal forecasting - I. Ba sic concept," *Tellus A*, vol. 57, pp. 219–233, 2005.

[98] S. Zhang, D. Li, and C. Qiu, "A multimodel ensemble-based kalman filter for the retrieval of soil moisture profiles," *Adv. Atmos. Sci.*, vol. 28, pp. 195–206, 2010.

[99] M. Jensen and Y. Yaari, "Role of intrinsic burst firing, potassium accumulation, and electrical coupling in the elevated potassium model of hippocampal epilepsy," *Journal of Neurophysiology*, vol. 77, pp. 1124–1233, 1997.

Curriculum Vitae

Franz Hamilton graduated from the International Baccalaureate program at Stonewall Jackson High School, Manassas, Virginia, in 2006. He received his Bachelor of Science in applied mathematics from George Mason University in 2010. The focus of his research has been on the intersection of data with mathematical modeling and the role of nonlinear data assimilation algorithms in understanding dynamical systems. His work has consisted of the following publications

1. **F. Hamilton**, T. Berry, T. Sauer. Predicting chaotic time series with a partial model (*Submitted to Physical Review E*)

2. **F. Hamilton**, R. Graham, L. Luu, N. Peixoto. Time-dependent increase in network response to stimulation (*Submitted to PLOS ONE*)

3. **F. Hamilton**, J. Cressman, N. Peixoto, T. Sauer. Reconstructing neural dynamics using data assimilation with multiple models. Europhysics Letters, 107, 68005 (2014)

4. **F. Hamilton**, A. Akhavian, G. Knaack, H. Charkhkar, S. Minnikanti, W. Kim, J. Kastee, N. Peixoto. Dynamic steering of in vitro cortical neurons using field stimulation. Engineering in Medicine and Biology Society (EMBC), 2014 36th Annual International Conference of the IEEE, 6577-6580 (2014).

5. **F. Hamilton**, T. Berry, N. Peixoto, T. Sauer. Real-time tracking of neuronal network structure using data assimilation. Physical Review E, 88, 052715 (2013)

6. G. Knaack, H. Charkhkar, **F. Hamilton**, N. Peixoto, T. O'Shaughnessy, J. Pancrazio. Differential response to ω-agatoxin IVA in murine frontal cortex and spinal cord derived neuronal networks. NeuroToxicology, 37, 19-25 (2013)

7. T. Berry, **F. Hamilton**, N. Peixoto, T. Sauer. Detecting connectivity changes in neuronal networks. Journal of Neuroscience Methods, 209, 388-397 (2012)

8. **F. Hamilton** and T. Sauer. Parameter estimation in differential equations: a numerical study of shooting methods. SIAM Undergraduate Research Online, 4 (2011)